Geophysical Journal International

Geophys. J. Int. (2010) **180,** 559–576 doi: 10.1111/j.1365-246X.2009.04460.x

Bending mechanics and mode selection in free subduction: a thin-sheet analysis

Neil M. Ribe

Univ Pierre et Marie Curie-Paris6, Univ Paris-Sud, CNRS Lab FAST, Bat 502, *Campus Univ, Orsay* F-91405, *France. E-mail: ribe@fast.u-psud.fr*

Accepted 2009 November 19. Received 2009 October 8; in original form 2009 July 1

SUMMARY

To elucidate the dynamics of free (buoyancy-driven) subduction of oceanic lithosphere, I study a model in which a 2-D sheet of viscous fluid with thickness h and viscosity $\gamma\eta_1$ subducts in an infinitely deep ambient fluid with viscosity η_1. Numerical solutions for the sheet's evolution are obtained using the boundary-element method (BEM), starting from an initial configuration comprising a short 'protoslab' attached to a longer horizontal 'plate' that is free to move laterally beneath an impermeable traction-free surface. Interpretation of the solutions using thin viscous sheet theory shows that the fundamental length scale controlling the subduction is the 'bending length' ℓ_b, defined at each instant as the length of the portion of the sheet's midsurface where the rate of change of curvature is significant. Geophysically speaking, ℓ_b is the sum of the lengths of the slab and of the region seaward of the trench where flexural bulging occurs. The bending length in turn enters into the definition of the sheet's dimensionless 'stiffness' $S \equiv \gamma(h/\ell_b)^3$, which controls whether the sinking speed of the slab is determined by the viscosity of the sheet itself ($S \gg 1$) or by that of the ambient fluid ($S \leq 1$). Motivated by laboratory observations of different modes of subduction (retreating versus advancing trench, folding versus no folding, etc.) in fluid layers with finite depth, I calculate numerically the dip θ_D of the slab's leading end as a function of γ and the normalized depth D/h to which it has penetrated. The contours of the function $\theta_D(\gamma, D/h)$ strongly resemble the intermode boundaries in the laboratory-based regime diagram of Schellart, supporting the hypothesis that the mode of subduction observed at long times in experiments is controlled by the dip of the slab's leading end when it reaches the bottom of the layer. In particular, the BEM solutions explain why trenches advance in the laboratory only when γ lies in an intermediate range, and why they retreat when γ is either smaller or larger than this. Application of the BEM model to Wu *et al.*'s compilation of the minimum curvature radii of subducted slabs suggests $\gamma \in [140, 510]$ for the Earth. This is too small to permit the laboratory-type 'trench advancing' mode, in agreement with the lack of tomographic evidence for slabs that are 'bent over backwards'.

Key words: Subduction zone processes; Dynamics of lithosphere and mantle; Mechanics, theory, and modelling.

1 INTRODUCTION

Subduction, defined as the sinking of dense (primarily oceanic) lithosphere into the Earth's mantle, is a major component of the planet's plate tectonic cycle. Its importance in global geodynamics is immense: it represents the main source of the buoyancy that drives mantle convection; it generates the majority of great earthquakes and explosive volcanoes on Earth; and it is the principal process responsible for recycling oceanic crust and volatile species such as water back into the mantle.

Yet despite subduction's obvious importance, the physical mechanisms underlying it have proven remarkably difficult to model convincingly. The main reason is that subduction exhibits two critical features that appear contradictory at first sight. On the one hand, subduction is driven by buoyancy forces alone, which act vertically and have no preference for 'right' or 'left'. Yet on the other hand, subduction on Earth is always laterally asymmetric or 'one-sided', with one plate plunging beneath another.

Faced with the difficulty of reconciling these two aspects, early models of subduction tended to focus on one at the expense of the other. The classic example of an asymmetric subduction model is the 'corner flow' model of McKenzie (1969), in which viscous flow in a wedge-shaped region is induced by an imposed motion of the wedge's inclined lower boundary (the 'subducting plate') in its own plane. This model elegantly embodies the one-sided character of real subduction zones; but the motion of the (non-deformable)

subducting plate is forced kinematically rather than being driven by negative buoyancy. At the opposite extreme is the influential free subduction model of Christensen & Yuen (1984), in which a dense slab with non-Newtonian rheology subducts within a self-consistent convective flow. This approach can model realistically the slab's deformation and its interaction with chemical and phase boundaries; but the subduction is perfectly symmetric.

A further step towards greater realism is represented by 'hybrid' models that include both free and forced aspects. In such models, which can be either analogue or numerical, the slab is typically allowed to subduct and deform freely, but a large-scale asymmetry is enforced by imposed geometric and/or kinematic constraints. A classic approach of this type is to force the subducting and/or overriding plates to move laterally with fixed velocities (e.g. Shemenda 1993; Houseman & Gubbins 1997; Becker *et al.* 1999; Faccenna *et al.* 1999; Schellart 2005; Billen & Hirth 2007; Heuret *et al.* 2007; Guillaume *et al.* 2009). Other parameters that can be imposed include the speed of trench retreat (Griffiths *et al.* 1995; Guillou-Frottier *et al.* 1995; Christensen 1996) and the geometry of lithospheric faults (e.g. Zhong & Gurnis 1996; Billen & Hirth 2007).

A still higher degree of realism is attained by 'free asymmetric' models in which one-sided subduction is driven by buoyancy alone, with no imposed geometric or kinematic constraints other than an asymmetric initial condition. Free asymmetric subduction has been modelled using three different approaches. The first is analogue laboratory experiments in which a flexible sheet (solid or high-viscosity fluid) sinks in a layer of low-viscosity fluid. The pairs of materials used in such experiments include rubber and water (Jacoby 1973), solid paraffin and molten paraffin (Jacoby 1976), very viscous and less viscous corn syrup (Kincaid & Olson 1987), and silicone putty and corn syrup (Funiciello *et al.* 2003b, 2004, 2008; Schellart 2004a,b, 2008; Bellahsen *et al.* 2005; Martinod *et al.* 2005; Faccenna *et al.* 2007). In a typical experiment, the sheet is first placed flat on the surface of the low-viscosity fluid, and one of its edges is then pushed downward to form a 'proto-slab' which initiates asymmetric subduction. This approach offers the advantage of inherent three-dimensionality, but considerable effort is required to characterize quantitatively the flow fields within the sheet and the ambient fluid (Funiciello *et al.* 2006; Schellart 2008).

A second approach is to solve the problem numerically, using full continuum descriptions of both the sheet and the ambient fluid. The sheet is defined by density and viscosity anomalies (diffusing or non-diffusing) that are prescribed initially in the form of a horizontal 'plate' with an attached proto-slab. The solutions obtained may be either steady-state (Conrad & Hager 1999), quasi-static (Piromallo *et al.* 2006), or fully time-dependent with an evolving sheet geometry (Schmeling *et al.* 1999; Enns *et al.* 2005; Morra & Regenauer-Lieb 2006; Morra *et al.* 2006; Stegman *et al.* 2006, 2009; Schellart 2007; Di Giuseppe *et al.* 2008; Ozbench *et al.* 2008; Schmeling *et al.* 2008). This approach guarantees a self-consistent treatment of the interaction of the sheet and its surroundings. But it is computationally expensive, and proper numerical treatment of the 'corner' region where the sheet separates from the upper surface is difficult (Schmeling *et al.* 2008).

The third approach, also numerical, is to represent the dynamics of the sheet and/or the surrounding mantle in a parametrized way that does not require explicit determination of the flow. One possibility is to calculate explicitly the flow within the sheet subject to a parametrized representation of the viscous stresses exerted by the surrounding mantle, using either a prescribed distribution of dashpots (Funiciello *et al.* 2003a) or drag coefficients derived from analytical solutions of the Stokes equations for idealized geometries (Royden & Husson 2006; Capitanio *et al.* 2007, 2009; Goes *et al.* 2008). Other options are to couple a parametrized representation of the sheet's bending deformation with an explicit calculation of the surrounding mantle flow (Conrad & Hager 2001) or to use parametrized representations for both the sheet and the surrounding mantle (Buffett & Rowley 2006). The main advantage of these approaches is their low computational cost, which allows the influence of different model parameters to be explored efficiently. However, the lack of an explicit flow field in part or all of the computational domain means that the interaction of the sheet with its surroundings cannot be treated with full self-consistency.

Taken together, the studies cited above represent a revolution in our understanding of subduction as a dynamically self-consistent process driven by buoyancy alone. They sketch a compelling picture of the two-way interaction of a slab with its surroundings, whereby a dense slab simultaneously drives mantle flow and is deformed by it. Moreover, the results of these studies provide convincing explanations for many features of the present and past geological record, including the correlation between trench velocity and plate velocity (Funiciello *et al.* 2008), the shapes of island arcs (Morra *et al.* 2006; Schellart *et al.* 2007), and episodes of lower-mantle slab penetration inferred from Cenozoic plate-motion histories (Goes *et al.* 2008). Yet despite this impressive progress, a basic understanding of the physical mechanisms underlying free asymmetric subduction is still lacking. In my view, there are three critical questions that remain to be answered.

The first question concerns the length scale that characterizes the bending deformation of a subducting viscous sheet in response to the gravitational and viscous forces acting on it. In an influential paper, Conrad & Hager (1999) proposed that the relevant length scale is the minimum value $R_{\min}$ of the sheet's radius of curvature R, an idea that has been further developed in more recent studies (e.g. Buffett 2006; Wu *et al.* 2008; Capitanio *et al.* 2009). Other authors take the radius of curvature at the trench as the fundamental length scale (Funiciello *et al.* 2003b; Bellahsen *et al.* 2005; Faccenna *et al.* 2007). By contrast, Royden & Husson (2006) treat slab bending without reference to R: the only length scales appearing in their model are the thickness of the upper mantle and the thickness, width and vertical deflection of the slab.

A second unresolved question concerns the proper measure of the mechanical resistance ('stiffness') of a subducting viscous sheet relative to that of the ambient mantle. Diverse answers to this question have been proposed in the literature. Conrad & Hager (1999) quantified the relative resistances of the sheet and the mantle by estimating the total rates of viscous dissipation within each. The ratio of the former to the latter is a dimensionless measure of the sheet's stiffness, and is $S \propto \gamma(h/R_{\min})^3$, where h is the plate thickness and γ is the ratio of the sheet viscosity to the mantle viscosity. A different approach was taken by Di Giuseppe *et al.* (2008), who estimated the sheet's stiffness from the position (in the model parameter space) of the boundary between modes of subduction with retreating and advancing trenches. They proposed a stiffness parameter $S = A \ln\gamma + Bh + C\Delta\rho$, where $\Delta\rho$ is the excess density of the sheet and $A > 0$, $B > 0$ and $C < 0$ are constants. Stegman *et al.* (2009) characterized the strength of the slabs in their 3-D numerical models using a normalized 'effective flexural stiffness' $S = \gamma(h/D)^3$, where D is the depth of the upper mantle. Finally, Capitanio *et al.* (2007) concluded on the basis of parametrized numerical models that a slab always sinks with the Stokes velocity appropriate for its (tabular) shape. This implies that the sheet's bending resistance can be neglected, that is, that its effective stiffness is zero.

The third open question concerns the origin of the different modes of free subduction seen in analogue laboratory experiments, which can be broadly classified according to whether the motion of the trench is retreating or advancing. Laboratory and numerical experiments suggest the 'rule of thumb' that the retreating mode is favoured when the plate is relatively thin, narrow (in the direction parallel to the trench), and dense, whereas thick, wide and less dense plates favour the advancing mode (Bellahsen *et al.* 2005; Di Giuseppe *et al.* 2008; Funiciello *et al.* 2008). A more quantitative laboratory-based phase diagram showing the mode of subduction as a function of the viscosity contrast γ and the ratio D/h of the layer depth to the sheet thickness was proposed by Schellart (2008). On the basis of 3-D numerical experiments, Stegman *et al.* (2009) proposed an alternative phase diagram for subduction modes as a function of the effective flexural stiffness $\gamma(h/D)^3$ and the (dimensional) 'Stokes buoyancy' $hg\Delta\rho/\eta_1$, where g is the gravitational acceleration and η_1 is the viscosity of the upper mantle. Di Giuseppe *et al.* (2008) suggested that the advancing mode is favoured for 'stiffer' sheets that cannot easily 'unbend' at depth; but their stiffness parameter $S = A \ln\gamma + Bh + C\Delta\rho$ does not reflect the physics of bending in any obvious way. In summary, it seems safe to say that the physical principle underlying mode selection in free subduction is not yet well understood.

The aim of this study is to propose quantitative answers to the three questions above, using a simple 2-D fluid mechanical model for the free subduction of a viscous sheet. The general approach is first to obtain highly accurate numerical solutions for the sheet's evolution as a function of its initial geometry and viscosity contrast, and then to interpret those solutions in light of the theory of thin viscous sheets. The model problem to be studied is described in the next section.

2 MODEL PROBLEM

Fig. 1 shows the geometry of the model, and Table 1 summarizes the notation used. The domain is an infinite fluid half-space with density ρ_1 and viscosity η_1, whose upper surface $x_2 = 0$ is both impermeable (zero normal velocity) and traction-free. Embedded within this layer is a sheet of fluid with density $\rho_2 > \rho_1$ and viscosity $\eta_2 \equiv \gamma\eta_1$ whose shape evolves with time. It comprises a horizontal piece (the 'plate') of length $L(t)$ and a bent piece (the 'slab') of length $\ell(t)$ whose leading end dips at an angle $\theta_0(t)$. At $t = 0$, the sheet has a uniform thickness h (excluding the rounded ends), and

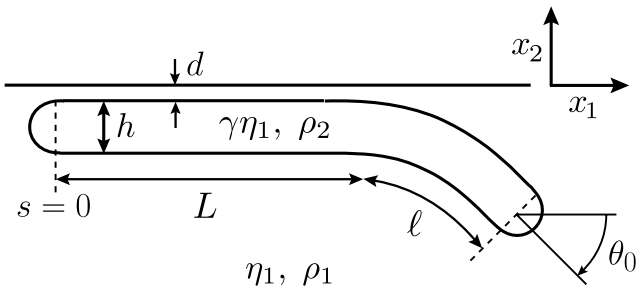

Figure 1. Model for free subduction of a 2-D sheet of fluid with viscosity $\gamma\eta_1$ and density $\rho_2 = \rho_1 + \Delta\rho$ in a half-space of fluid with viscosity η_1 and density ρ_1. The symbols h and d indicate the initially constant thicknesses of the sheet and the thin 'lubrication layer' of fluid above its horizontal portion. As subduction proceeds, the thicknesses of the sheet and the lubrication layer become spatially non-uniform, and L, ℓ and θ_0 vary in time. $s \in [0, L + \ell]$ is the arclength coordinate along the sheet's midsurface. The upper surface $x_2 = 0$ is impermeable and free of shear traction.

the upper surface of the plate is at $x_2 = -d$. The sheet's 'midsurface' lies midway between its upper and lower surfaces. The arclength along the midsurface is $s \in [0, L(t) + \ell(t)]$, such that $s = 0$ and $s = L(t)$ correspond to the 'ridge' and the 'trench', respectively. By convention, the midsurface is defined only within the portion of the sheet having uniform thickness, and does not extend into the rounded ends (see Fig. 1). At $t = 0$, the dip $\theta(s, 0)$ (clockwise from horizontal) of the 'slab' portion of the midsurface is

$$\theta(s, 0) = \theta_0(0)s^2[3\ell(0) - 2s]/\ell(0)^3. \quad (1)$$

Eq. (1) implies that the midsurface curvature $K(s) \equiv -\partial_s\,\theta(s, 0)$ is initially zero at both the slab's leading end $s = L(0) + \ell(0)$ and the trench $s = L(0)$ (where the curvature must vanish to match that of the plate.) Finally, the shape of the two rounded ends is chosen to ensure continuous curvature at the points where they join with the rest of the sheet. The entire outer surface of the sheet is denoted by the symbol C.

Because the model problem of Fig. 1 is 2-D, the existence of a solution is not immediately obvious and needs to be justified explicitly. It is well known that the equations for slow 2-D viscous flow around an infinitely long cylinder sinking in an unbounded fluid have no solution (Stokes's paradox). This is true regardless of whether the cylinder is solid or fluid, and is also independent of the shape of its cross-section. The origin of the paradox is the fact that the 2-D velocity field due to an infinite line force diverges logarithmically at large distances, which implies that the Stokes equations have no bounded solution if the total force acting on the fluid is non-zero. However, it also implies that a solution will exist if the domain is modified in such a way that the total force on the fluid becomes zero. A simple way to do this is to replace the original infinite domain by a half-space bounded by an impermeable horizontal surface $x_2 = 0$, as in Fig. 1. In this new configuration, the total downward force exerted on the ambient fluid by the sinking sheet is exactly balanced by the integral of the normal stresses acting on the surface $x_2 = 0$. The net force on the ambient fluid is therefore zero and a bounded solution of the Stokes equations exists, even though the ambient fluid extends downward to infinity.

Finally, the role of the thin layer of low-viscosity fluid above the plate in Fig. 1 requires some comment. If an isolated sheet of dense viscous fluid comprising a horizontal 'plate' and a submerged 'slab' is placed on top of a less dense fluid, the natural tendency of the plate, no less than that of the slab, is to sink. This tendency must somehow be counteracted if the plate is to move in an 'earthlike' way, that is, laterally but not vertically. In the Earth, the sinking of each plate is inhibited by the presence of its neighbours, which prevents the underlying mantle from welling up between the plates and spreading over them. If however our goal is to model the behaviour of an isolated sheet with free edges, then some additional force is required to hold up the plate. In the case of laboratory experiments, which typically involve sheets of silicone putty subducting in honey, that force is probably surface tension acting along the three-phase contact lines where silicone putty, honey and air meet. This idea is supported by a laboratory experiment in which the 'standard' protocol of Bellahsen *et al.* (2005) is slightly but significantly modified (F. Funiciello, personal communication, 2007). A rectangular sheet of silicone putty with dimensions 20 × 35 × 1.2 cm was placed flat on the surface of a tank of honey and left there. After 7 hr during which the sheet remained in place without sinking, its upper surface was lightly painted with honey, and one of its edges was pushed 2 cm down into the honey filling the tank. But instead of exhibiting the typical subduction-like behaviour documented by Bellahsen *et al.* (2005), the whole sheet sank beneath the surface of

Table 1. Notation.

Variable	Definition	Units	Defined in
d	Lubrication layer thickness	m	Fig. 1
D	Layer depth or reference depth	m	
D_{90}	Depth of the slab's leading end when $\theta_0 = 90^\circ$	m	Fig. 4
$\hat{D}_{90}$	Reduced value (midsurface deflection) of D_{90}	m	Fig. 4; eq. (C2)
g	Gravitational acceleration	m s^{-2}	
h	Plate thickness	m	Fig. 1
K	$\equiv -\partial\theta/\partial s$; midsurface curvature	m^{-1}	
$\dot{K}$	Rate of change of midsurface curvature	m^{-1} s^{-1}	Eq. (15)
ℓ	Slab length	m	Fig. 1
$\dot{\ell}$	Subduction rate	m s^{-1}	Section 4
ℓ_b	Bending length	m	Fig. 5
L	Plate length	m	Fig. 1
M	Bending moment	kg m s^{-2}	Eq. (16)
R	$\equiv 1/\|K\|$; Radius of curvature of the midsurface	m	
$R_{\min}$	Minimum value of R	m	
s	Arclength along the midsurface	m	Fig. 1
S	Sheet stiffness	None	Eq. (18)
t	Time	s	
u_1^{tip}	Horizontal velocity of the slab tip	m s^{-1}	
U	Longitudinal velocity of the midsurface	m s^{-1}	Fig. 4
U_p	Plate speed	m s^{-1}	Section 4
U_{trench}	$\equiv U_0 - \dot{\ell}$; trench speed	m s^{-1}	Section 4
V	Sinking speed of the slab's tip	m s^{-1}	Section 4
V_{Stokes}	Characteristic Stokes sinking speed	m s^{-1}	Eq. (10)
w	Sheet width	m	
W	Normal velocity of the sheet's midsurface	m s^{-1}	Fig. 4
γ	$\equiv \eta_2/\eta_1$; viscosity contrast	None	Fig. 1
$\Delta\rho$	$\equiv \rho_2 - \rho_1$; excess sheet density	kg m^{-3}	Fig. 1
η_1	Ambient mantle viscosity	Pa s	Fig. 1
η_2	Sheet viscosity	Pa s	Fig. 1
θ	Dip of the midsurface	None	Eq. (1)
θ_0	Dip of the slab's leading end	None	Fig. 1
θ_D	Dip of the slab's leading end when its depth is D	None	
ρ_1	Ambient mantle density	kg m^{-3}	Fig. 1
ρ_2	Sheet density	kg m^{-3}	Fig. 1

the honey within a few tens of minutes. Because the effect of the painting is to eliminate the highly curved meniscus at the contact line, the experiment seems to suggest that surface tension acting on this meniscus provided the upward force required to balance the sheet's negative buoyancy during the first 7 hr of the experiment. The critical role played by surface tension in analogue experiments on free subduction has also been noted by Jacoby (1976).

However, the importance of surface tension in the laboratory does not mean that it should be included in numerical models; and if it is not, then some other means of supporting the plate is necessary. One possibility is to impose a condition of zero normal velocity at the plate's upper surface; but it then becomes necessary to modify the rheology of the sheet near the trench in an *ad hoc* way to get it to subduct (e.g. Enns *et al.* 2005; Di Giuseppe *et al.* 2008; Stegman *et al.* 2009). Another possibility is to support the plate by imposing isostatic restoring forces along its base (e.g. Funiciello *et al.* 2003a; Capitanio *et al.* 2007, 2009). A third possibility, and the one I have chosen here, is to interpose a thin 'lubrication layer' of low-viscosity fluid between the plate and the surface $x_2 = 0$, which is assumed to be both impermeable and free of shear traction (Fig. 1). According to a standard result from lubrication theory, normal stresses greatly exceed shear stresses within the lubrication layer. The plate is thus free to move horizontally, but its sinking is impeded by a strong upward-directed normal stress whose value throughout the plate's interior (away from the ends of the lubrication layer) is $hg\Delta\rho$ (Appendix B). The lubrication layer can therefore be regarded simply as a mechanism for maintaining the plate in a state of perfect local isostatic equilibrium while allowing it to move freely in response to the pull of a freely deforming slab. Similar lubrication layers have also been used in other numerical models of free subduction (Morra *et al.* 2007; Ozbench *et al.* 2008; Schmeling *et al.* 2008).

To summarize, the model geometry shown in Fig. 1 offers several significant advantages. First, the flow fields within both the sheet and the ambient fluid are regular in the vicinity of the trench, allowing subduction to occur freely with no need for *ad hoc* modifications of the rheology. Second, the presence of the lubrication layer allows flexural bulging of the plate to occur seaward of the trench, an effect whose importance will become clear below. Finally, the smoothness of the interface between the two fluids permits the use of an efficient and highly accurate numerical method, described next.

3 NUMERICAL METHOD

Because inertia is negligible, the flow within the sheet and in the fluid surrounding it is entirely determined at each instant by the current geometry of the interface. Problems of this type can be efficiently solved using a boundary-integral representation, whereby slow viscous flow in a given region is expressed by weighted integrals of the tractions and velocities on the boundaries of that region.

Pozrikidis (1990) and Manga & Stone (1993) derived the appropriate boundary-integral representation for the general case of a buoyant 'drop' of fluid entirely surrounded by a second fluid with a different viscosity, of which the system of Fig. 1 is an example. Let $V_i (i = 1 \text{ or } 2)$ be the region occupied by the fluid with viscosity η_i, and let C be the interface between the two fluids. Furthermore, let $u^{(i)}(\boldsymbol{x})$ $(i = 1 \text{ or } 2)$ be the fluid velocity at the point $\boldsymbol{x}$ in V_i, such that $u^{(1)}(\boldsymbol{x}) = u^{(2)}(\boldsymbol{x})$ for $\boldsymbol{x} \in C$. Then the velocities $u^{(i)}(\boldsymbol{x})$ satisfy

$$\chi_1(\boldsymbol{x})\boldsymbol{u}^{(1)}(\boldsymbol{x}) + \gamma\chi_2(\boldsymbol{x})\boldsymbol{u}^{(2)}(\boldsymbol{x}) - (1-\gamma) \times \int_C \boldsymbol{u}(\boldsymbol{y})\cdot\boldsymbol{K}(\boldsymbol{y}-\boldsymbol{x})\cdot\boldsymbol{n}(\boldsymbol{y})\mathrm{d}\ell(\boldsymbol{y}) = -\frac{\Delta\rho}{\eta_1}\int_C (\boldsymbol{g}\cdot\boldsymbol{y})\boldsymbol{n}(\boldsymbol{y})\boldsymbol{J}(\boldsymbol{y}-\boldsymbol{x})\mathrm{d}\ell(\boldsymbol{y}), \tag{2}$$

where $\boldsymbol{J}$ and $\boldsymbol{K}$ are Green's functions and $\boldsymbol{n}$ is the unit normal to C that points out of the sheet. $\chi_1(\boldsymbol{x}) = 0$, 1/2, or 1 if $\boldsymbol{x}$ is in V_2, right on C, or in V_1, respectively, and $\chi_2(\boldsymbol{x})$ is defined similarly but with the subscripts 1 and 2 interchanged.

The Green's functions $\boldsymbol{J}$ and $\boldsymbol{K}$ are singular solutions of the Stokes equations that represent the velocity and stress, respectively, at $\boldsymbol{y}$ due to a line force at $\boldsymbol{x}$, and which satisfy automatically the boundary conditions at $x_2 = 0$. Their explicit forms are

$$J_{ij}(\boldsymbol{y}-\boldsymbol{x}) = J^{\star}_{ij}(\boldsymbol{y}-\boldsymbol{x}) + (-1)^{j+1}J^{\star}_{ij}(\boldsymbol{y}-\boldsymbol{x}^{\mathrm{IM}}), \tag{3a}$$

$$K_{ij}(\boldsymbol{y}-\boldsymbol{x}) = K^{\star}_{ij}(\boldsymbol{y}-\boldsymbol{x}) + (-1)^{j+1}K^{\star}_{ij}(\boldsymbol{y}-\boldsymbol{x}^{\mathrm{IM}}), \tag{3b}$$

where $\boldsymbol{x}^{\mathrm{IM}} \equiv \boldsymbol{x} - 2\,x_2\,\boldsymbol{e}_2$ is the mirror image of the point $\boldsymbol{x}$ across the boundary $x_2 = 0$ and

$$J^{\star}_{ij}(\boldsymbol{r}) = \frac{1}{4\pi}\left(-\delta_{ij}\ln|\boldsymbol{r}| + \frac{r_i r_j}{|\boldsymbol{r}|^2}\right), \quad K^{\star}_{ij}(\boldsymbol{r}) = -\frac{1}{\pi}\frac{r_i r_j r_k}{|\boldsymbol{r}|^4} \tag{4}$$

are the Green's functions for a line force in an infinite fluid.

For points $\boldsymbol{x}$ on C, (2) is a Fredholm integral equation of the second kind for the velocity $\boldsymbol{u}$ of the interface. Once $\boldsymbol{u}$ on C is known, $\boldsymbol{u}$ at other points $\boldsymbol{x}$ can be determined by evaluating the integrals in (2) with $\chi_1 = 1$ and $\chi_2 = 0$ (if $\boldsymbol{x} \in V_1$) or $\chi_1 = 0$ and $\chi_2 = 1$ (if $\boldsymbol{x} \in V_2$.) Finally, the position of each material point $\boldsymbol{x}$ on the interface evolves according to

$$\frac{\mathrm{d}\boldsymbol{x}}{\mathrm{d}t} = \boldsymbol{u}(\boldsymbol{x}). \tag{5}$$

The dimensionless parameters that control the dynamics of the system can be identified by rewriting (2) and (5) in terms of the dimensionless variables

$$(\hat{x}, \hat{y}) = h^{-1}(x, y), \quad \hat{\boldsymbol{u}} = \frac{\eta_1}{h^2 g\Delta\rho}\boldsymbol{u}, \quad \hat{t} = \frac{hg\Delta\rho}{\eta_1}t. \tag{6}$$

The results are

$$\chi_1(\boldsymbol{x})\boldsymbol{u}^{(1)}(\boldsymbol{x}) + \gamma\chi_2(\boldsymbol{x})\boldsymbol{u}^{(2)}(\boldsymbol{x}) - (1-\gamma) \times \int_C \boldsymbol{u}(\boldsymbol{y})\cdot\boldsymbol{K}(\boldsymbol{y}-\boldsymbol{x})\cdot\boldsymbol{n}(\boldsymbol{y})\mathrm{d}\ell(\boldsymbol{y}) = \int_C (\boldsymbol{e}_2\cdot\boldsymbol{y})\boldsymbol{n}(\boldsymbol{y})\boldsymbol{J}(\boldsymbol{y}-\boldsymbol{x})\mathrm{d}\ell(\boldsymbol{y}), \tag{7}$$

$$\frac{\mathrm{d}\boldsymbol{x}}{\mathrm{d}t} = \boldsymbol{u}(\boldsymbol{x}), \tag{8}$$

where $\boldsymbol{e}_2$ is the (upward-pointing) vertical unit vector and the hat symbols have been suppressed to simplify the notation. The only dimensionless parameters that appear in (7) and (8) are the viscosity contrast γ and the four parameters that define the shape of the contour C, which I shall take to be $L(0)/\ell(0)$, $\ell(0)/h$, d/h and $\theta_0(0)$. Accordingly, the velocity $\boldsymbol{u}(\boldsymbol{x})$ for $\boldsymbol{x} \in C$ must have the general form

$$\frac{\boldsymbol{u}}{V_{\mathrm{Stokes}}} = \mathrm{fct}\left[\frac{\boldsymbol{x}}{h}, \frac{hg\Delta\rho}{\eta_1}t, \gamma, \frac{L(0)}{\ell(0)}, \frac{\ell(0)}{h}, \frac{d}{h}, \theta_0(0)\right], \tag{9}$$

where

$$V_{\mathrm{Stokes}} = \frac{h\ell(0)g\Delta\rho}{\eta_1} \tag{10}$$

is the characteristic Stokes sinking velocity scale for a thin object (e.g. a coin) with thickness h and lateral dimension $\ell(0) \gg h$. Eq. (9) is the basis for the subsequent dimensional analysis of several aspects of subduction dynamics.

The numerical solution procedure for (7) and (8) is as follows. First, the integrals in (7) are regularized by 'subtracting the singularity' at $\boldsymbol{y} = \boldsymbol{x}$ following the method outlined in section 6.4 of Pozrikidis (1992), which yields

$$\int_C (\boldsymbol{g}\cdot\boldsymbol{y})\boldsymbol{n}(\boldsymbol{y})\cdot\boldsymbol{J}(\boldsymbol{y}-\boldsymbol{x})\mathrm{d}\ell(\boldsymbol{y}) = \int_C [\boldsymbol{g}\cdot(\boldsymbol{y}-\boldsymbol{x})]\boldsymbol{n}(\boldsymbol{y})\cdot\boldsymbol{J}(\boldsymbol{y}-\boldsymbol{x})\mathrm{d}\ell(\boldsymbol{y}), \tag{11a}$$

$$\int_C \boldsymbol{u}(\boldsymbol{y})\cdot\boldsymbol{K}(\boldsymbol{y}-\boldsymbol{x})\cdot\boldsymbol{n}(\boldsymbol{y})\mathrm{d}\ell(\boldsymbol{y}) = \int_C [\boldsymbol{u}(\boldsymbol{y}) - \boldsymbol{u}(\boldsymbol{x})]\cdot\boldsymbol{K}(\boldsymbol{y}-\boldsymbol{x})\cdot\boldsymbol{n}(\boldsymbol{y})\mathrm{d}\ell(\boldsymbol{y}) - \frac{1}{2}\boldsymbol{u}(\boldsymbol{x}). \tag{11b}$$

Next, the contour C is discretized using three-node curved elements C_n $(n = 1, 2, \ldots, N)$, over each of which $\boldsymbol{y}$, $\boldsymbol{n}$ and $\boldsymbol{u}$ vary as

$$\boldsymbol{y}(\xi) = \sum_{m=1}^{3}\phi_m(\xi)\boldsymbol{y}_m, \quad \boldsymbol{n}(\xi) = \frac{\partial_\xi \boldsymbol{y}\times\boldsymbol{e}_3}{|\partial_\xi \boldsymbol{y}\times\boldsymbol{e}_3|},$$
$$\boldsymbol{u}(\xi) = \sum_{m=1}^{3}\phi_m(\xi)\boldsymbol{u}_m, \tag{12}$$

where $\boldsymbol{y}_m$ are the (known) nodal coordinates, $\boldsymbol{u}_m$ are the (unknown) nodal velocities, and $\phi_m(\xi)$ are quadratic basis functions defined on a 'master' element $\xi \in [-1, 1]$. Substitution of (12) into (7) with $\boldsymbol{x} \in C$ transforms the integrals over C into sums of integrals over the elements C_n, each of which is evaluated on $\xi \in [-1, 1]$ using 6-point Gauss–Legendre quadrature. The resulting system of $4N$ coupled linear equations is solved iteratively using the biconjugate gradient algorithm of Press *et al.* (1996), yielding the nodal velocities $\boldsymbol{u}_m$ with fourth-order accuracy. The positions of all material points $\boldsymbol{x} \in C$ are then advanced in time by solving (5) using a second-order Runge–Kutta (midpoint) method. The accuracy of the (instantaneous) velocity determination was verified against two independent solutions for the flow due to a cylinder moving normal to an impermeable traction-free surface: an analytical solution valid in the limit $\gamma \to \infty$ (Wakiya 1975), and an integral representation valid for $\gamma = 1$. The accuracy of the time stepping was checked by monitoring the area enclosed by the contour C, which was constant to within 0.01 per cent in all cases. Doubling the (spatial and/or temporal) resolution yielded results indistinguishable from those shown below to within the width of the plotting lines.

4 SIMULATIONS OF UNSTEADY SUBDUCTION

To provide some initial understanding, I begin by examining some qualitative features of the behaviour of the model system, focussing

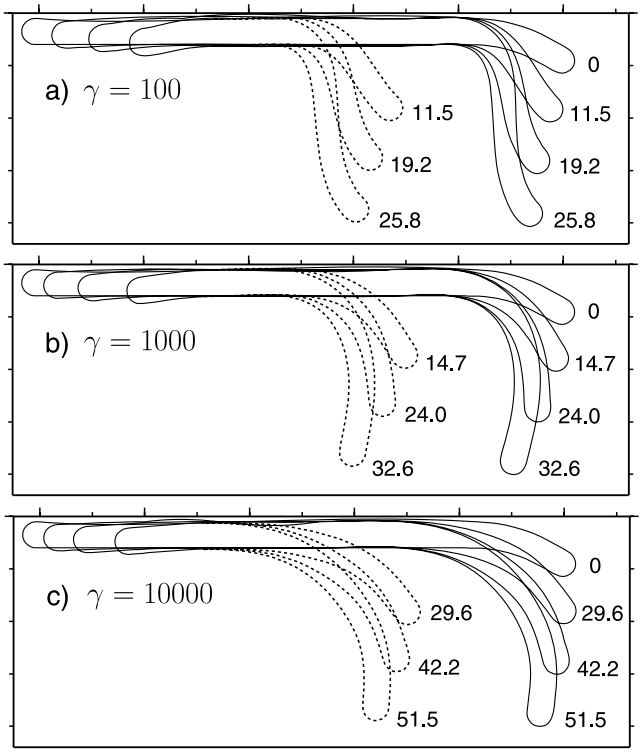

Figure 2. Time evolution of freely subducting sheets for three values of the viscosity contrast γ. Solid lines: shapes of the sheet at the dimensionless times $thg\Delta\rho/\eta_1$ indicated, starting from the initial conditions $L(0) = 16h$, $\ell(0) = 4h$, $d = 0.2h$ and $\theta_0(0) = 30°$. Dashed lines: shapes at the same times for a longer plate with $L(0) = 32h$ (displayed at an arbitrary horizontal position).

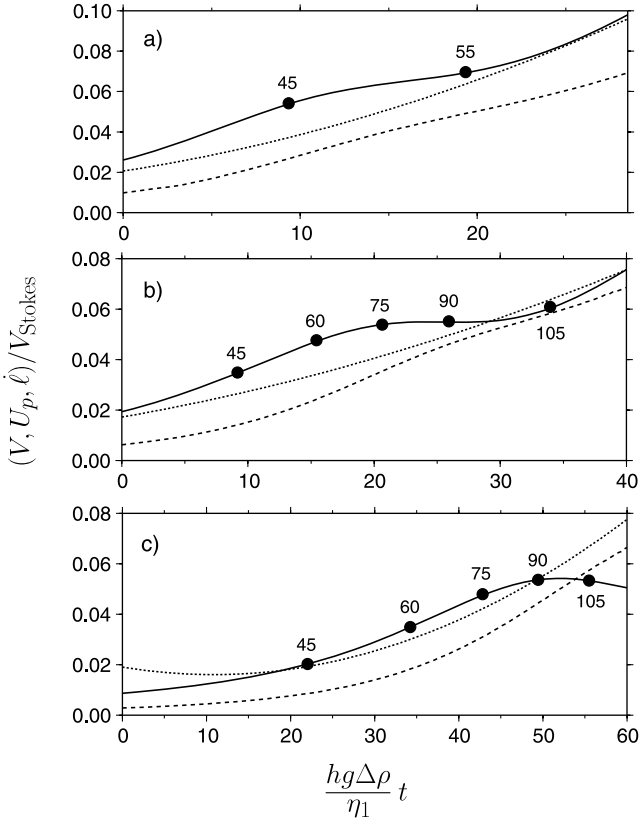

Figure 3. Characteristic velocities for the three solutions of Fig. 2 as functions of time. Solid lines: sinking speed V. Dashed lines: plate speed U_p. Dotted lines: subduction rate $\dot{\ell}$. The dots along the solid curves indicate the dip of the leading end of the slab in degrees.

on the influence of the plate/mantle viscosity contrast γ. The solid lines in Fig. 2 show the time evolution of a sheet starting from the initial conditions $L(0) = 16h$, $\ell(0) = 4h$, $d = 0.2h$ and $\theta_0(0) = 30°$, for $\gamma = 100$ (Fig. 2a), 1000 (Fig. 2b) and 10 000 (Fig. 2c). For each value of γ, the sheet's shape is displayed at the times at which the depth of the slab tip is 2.04 h (the initial condition), $4h$, $6h$ and $8h$, respectively. The corresponding values of the dimensionless time $thg\Delta\rho/\eta_1$ are indicated. The style of subduction depends strongly on γ. The weakest sheet ($\gamma = 100$) curls counter-clockwise at the trench while its lowermost part curls clockwise in response to the stresses applied by the mantle flowing around the slab tip. The 'plate' portion of the sheet moves steadily to the right while the trench retreats (but more slowly) to the left. For $\gamma = 10^3$ (Fig. 2b), the curling of the slab is no longer concentrated near the trench, and is counter-clockwise along the whole length of the slab. Once bent, the slab is difficult to unbend because the gravitational force acting on it is dominantly parallel to the midsurface. The dip of the slab's lower part therefore overshoots the vertical to values $> 90°$. Similar behaviour is observed for $\gamma = 10^4$ (Fig. 2c).

To illustrate the influence of the initial plate length $L(0)$, Fig. 2 also shows the evolution of a longer sheet with $L(0) = 32\ h$ but the same initial values of $\ell(0)$, d and θ_0 (dashed lines). These shapes are shown at the same dimensionless times as those for $L(0) = 16\ h$, but at an arbitrary horizontal position to facilitate comparison. The differences are minor, demonstrating that the evolution of the slab shape is nearly independent of the plate length.

The results of Fig. 2 can be quantified in more detail by defining three characteristic velocities. The first is the vertical 'sinking speed' $V \equiv -\boldsymbol{u} \cdot \boldsymbol{e}_2 > 0$ of the leading edge of the subducting slab. The second is the 'plate speed' U_p, defined as the average rightward velocity of the portion of the sheet whose upper and lower surfaces are horizontal to within 1°. The third is the 'subduction rate' $\dot{\ell}$, that is, the rate at which the plate is consumed by subduction. It was determined numerically from the rate of increase of the total amount of slab material located below the depth $x_2 = -h - d$ that corresponds to the base of the plate.

Fig. 3 shows the velocities $V(t)$, $U_p(t)$ and $\dot{\ell}(t)$ as functions of time for the three solutions of Fig. 2. To a first approximation, all the velocities increase with time due to the steadily increasing negative buoyancy ('slab pull') of the lengthening slab. The trench velocity $U_{\rm trench} \equiv U_p - \dot{\ell}$ is always negative, indicating leftward (retreating) trench motion. The ratio $|U_{\rm trench}/U_p|$ (trench velocity as a fraction of plate velocity) increases as a function of γ for $t = 0$, and decreases as a function of time for fixed γ.

5 THIN-SHEET SCALING ANALYSIS

The next task is to uncover the physical mechanisms and scaling laws that underly the complex behaviour shown in Figs 2 and 3. The first point to note is that because inertia is negligible, the evolutionary history of a subducting sheet is nothing more than a sequence of quasi-static configurations whose dynamics are determined entirely by the sheet's instantaneous shape. It therefore makes sense first to study the quasi-static dynamics of a sheet as a function of its viscosity contrast and shape, without the added complexity of the (purely kinematic) time evolution. To do this, I shall use as a 'reference' configuration the geometry shown in Fig. 1, together with the

analytical form (1) for the dip $\theta(s, 0)$ of the midsurface. But instead of regarding $L(0)$, $\ell(0)$ and $\theta_0(0)$ as 'initial' values in a time-dependent simulation, I shall treat them as free geometrical parameters that can be varied to represent a wide range of different sheet shapes at some arbitrary instant in time. Accordingly, in this section I consider only instantaneous solutions of the boundary-integral eq. (7), and ignore the time evolution described by the kinematic eq. (8). The notation is simplified by suppressing the time argument on all parameters, writing e.g. L instead of $L(0)$, etc.

As the first 'target' parameter for the scaling analysis, consider the sinking speed V of the slab. Because V is an instantaneous quantity defined at a particular material point on the sheet, it depends neither on t nor on $\boldsymbol{x}$. Moreover, the numerical solutions show that V is very nearly independent of L: it changes by <1 per cent when L is increased from $16h$ to $32h$. The general relation (9) then reduces to

$$\frac{V\eta_1}{h\ell g\Delta\rho} = \text{fct}\left(\gamma, \frac{\ell}{h}, \frac{d}{h}, \theta_0\right). \tag{13}$$

I emphasize here that a relation of the form (13) is valid only for the 'vertical' component V of the slab tip velocity, and *not* for its horizontal component u_1^{tip}, which *does* depend on L. The dependence of u_1^{tip} on L is what accounts for the minor differences between the time evolutions of sheets with different values of $L(0)$ in Fig. 2. The reason why u_1^{tip} depends on L is that it includes a contribution from the plate speed U_p, which itself depends on L because it is influenced by the drag exerted on the plate by the underlying mantle. The dependence of U_p on L is quantified in more detail below.

The functional dependence in (13) could be determined by the 'brute force' method of obtaining numerical solutions over a grid in the 4-D parameter space $(\gamma, \ell/h, d/h, \theta_0)$, but the result would not provide any physical insight. A better approach is to interpret the numerical solutions with the help of physical scaling arguments derived from the theory of thin viscous sheets (Buckmaster *et al.* 1975; Ribe 2001, 2002; Buffett 2006). In this theory, the dynamics of a sheet are described entirely in terms of quantities defined on its midsurface. For a 2-D sheet, the basic quantities are the components $U(s)$ and $W(s)$ of the velocity in the directions parallel to and normal to the midsurface, respectively (Fig. 4). Next, the rates of stretching (Δ) and rotation (ω) of the midsurface are defined as

$$\Delta = U' - KW, \qquad \omega = W' + KU, \tag{14}$$

where (to repeat) $K(s)$ is the curvature of the midsurface and primes denote $\mathrm{d}/\mathrm{d}s$. A final derived quantity is the rate of change of the midsurface curvature (Ribe 2003)

$$\dot{K} = \omega' - K\Delta, \tag{15}$$

which will be called the 'curling rate' for short. Note that the rates of stretching, rotation and curling defined by (14) and (15) are all advective rates of change following the motion of a material point on the midsurface.

The curling rate is a direct measure of the internal stresses that resist the bending of the sheet, as one sees immediately from the formula for the bending moment (Ribe 2001)

$$M = -\frac{1}{3}\eta_2 h^3 \dot{K}. \tag{16}$$

$\dot{K}$ is determined from the BEM numerical solutions by first calculating $U(s)$ and $W(s)$ from (7) with $\chi_1 = 0$, $\chi_2 = 1$ for points $\boldsymbol{x}(s)$ located on the sheet's midsurface, and then evaluating numerically the derivatives in (14) and (15). Fig. 5 shows $\dot{K}(s)$ for the initial ($t = 0$) configuration of the three sheets whose time evolution is shown in Fig. 2. In each case, the 'slab' portion of the sheet corresponds to $s > 16$. For the weakest sheet ($\gamma = 100$; solid line), the upper part of the slab curls clockwise ($\dot{K} < 0$), as one would expect for bending under gravity. The lower part, however, curls in the opposite direction due to the tractions applied by the mantle 'wind' flowing around the tip of the slab. For the stiffer sheets ($\gamma = 10^3$ and 10^4; dashed and dotted lines), the tractions applied by the mantle wind are too weak to influence all but the lowermost tip of the slab, so the slab curls clockwise over nearly

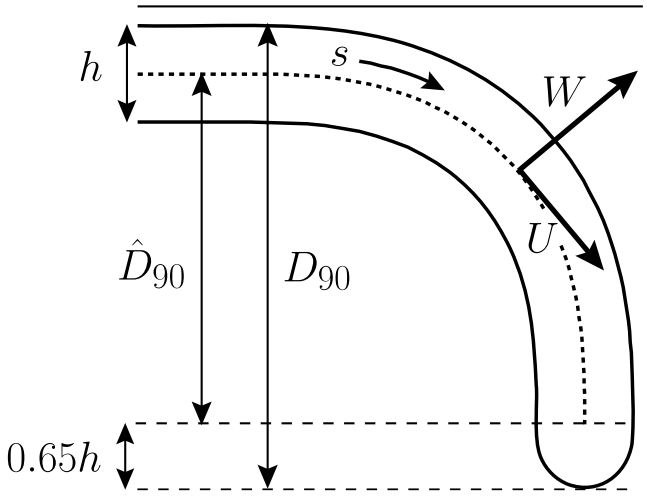

Figure 4. Definitions of parameters characterizing a thin viscous sheet. The sheet's midsurface is indicated by the dotted line, and s is the arclength coordinate along it. $U(s)$ and $W(s)$ are the components of the fluid velocity at points on the midsurface in the directions parallel and perpendicular to it, respectively, and are positive in the senses indicated. For the special case of a slab whose leading end is vertical, D_{90} is the maximum depth of the slab below the upper surface of the plate, and $\hat{D}_{90} \equiv D_{90} - 1.15h$ is the total vertical deflection of the midsurface. The sheet's thickness h and the length ($= 0.65h$) of the slab's endpiece remain nearly constant during progressive subduction when $\gamma \geq 100$.

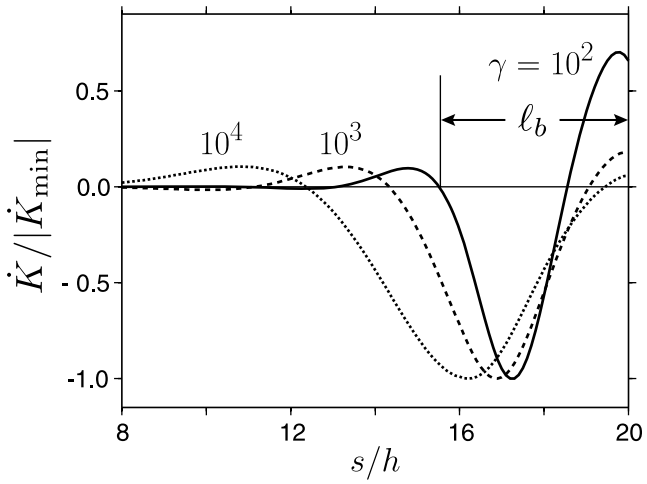

Figure 5. Rate of curling $\dot{K}(s)$ as a function of arclength for the sheets of Fig. 2 at the initial instant $t = 0$. The solid, dashed, and dotted lines are for $\gamma = 100$, 1000 and 10^4, respectively. The corresponding minimum values of $\eta_1\dot{K}/g\Delta\rho$ are -0.0281, -0.010 and -0.00246, respectively. The definition of the bending length ℓ_b is indicated for $\gamma = 100$.

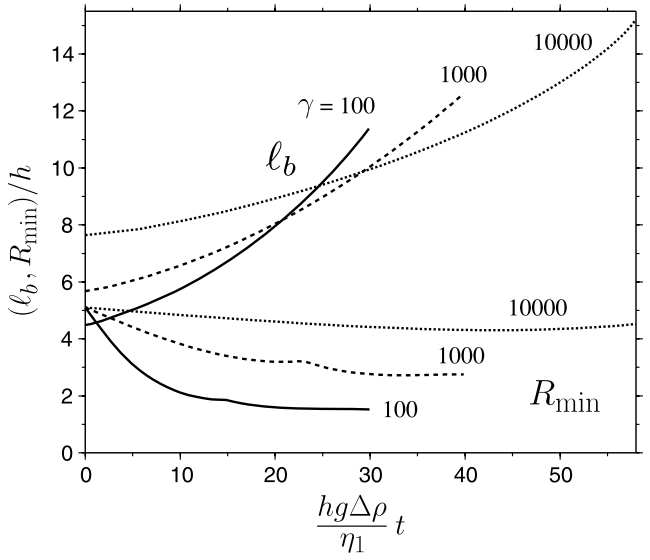

Figure 6. Time evolution of the bending length $\ell_b(t)$ (upper curves) and the minimum radius of curvature $R_{\min}(t)$ for the three simulations of Fig. 2. The viscosity contrast γ for each curve is indicated.

its whole length. Moreover, significant bending also occurs seaward of the trench, over a distance that increases with increasing γ. The 'flexural bulge' produced by this bending is observed seaward of many trenches on Earth (Watts & Talwani 1974; Turcotte *et al.* 1978).

Motivated by the curves of Fig. 5, I now define the 'bending length' ℓ_b as the length of the portion of the sheet's midsurface where the curling rate $\dot{K}(s)$ is significantly different from zero. To make this definition mathematically precise in the context of the present model, I take ℓ_b to be the distance from the end of the sheet's midsurface (excluding the rounded 'endcap') to the first zero of $\dot{K}(s)$ to the left-hand side of the point where this function has its global minimum. This definition is illustrated in Fig. 5 for the curve $\dot{K}(s)$ at the initial instant of the simulation with $\gamma = 100$ in Fig. 2. However, the bending length is also defined at all later instants, and typically increases monotonically with time because the slab is continually lengthening. Fig. 6 shows this for the three simulations of Fig. 2. For comparison, Fig. 6 also shows the sheet's minimum radius of curvature $R_{\min}(t)$ for the same three simulations. Unlike $\ell_b(t)$, $R_{\min}(t)$ initially decreases and then increases more slowly. These contrasting behaviours show that the length scales $\ell_b(t)$ and $R_{\min}(t)$ are fundamentally different in character, as discussed in more detail in Section 8.

With the definition of ℓ_b in hand, I now consider the balance of forces (per unit length in the x_3-direction) acting on the bending portion of the sheet at an arbitrary instant in time. The traction σ_1 applied to this portion by the outer fluid is $\sigma_1 \sim \eta_1 V/\ell_b$, which implies a total (integrated with respect to arclength) force $F_1 \sim \eta_1 V$. Thin-sheet theory (Ribe 2001) shows that the internal traction σ_2 that resists the bending is $\sigma_2 \sim M'' \sim \eta_2\, h^3 V/\ell_b^4$, which corresponds to a force $F_2 \sim \eta_2 h^3 V/\ell_b^3$. Finally, because the negative buoyancy of the 'plate' portion of the sheet is compensated by normal stresses in the lubrication layer, the effective buoyancy force $F_b \sim h\ell g\Delta\rho$ is due entirely to the slab portion of length ℓ. In the limit of negligible bending resistance, the balance $F_b \sim F_1$ implies

$$V \sim \frac{h\ell g\Delta\rho}{\eta_1} \equiv V_{\text{Stokes}}. \tag{17}$$

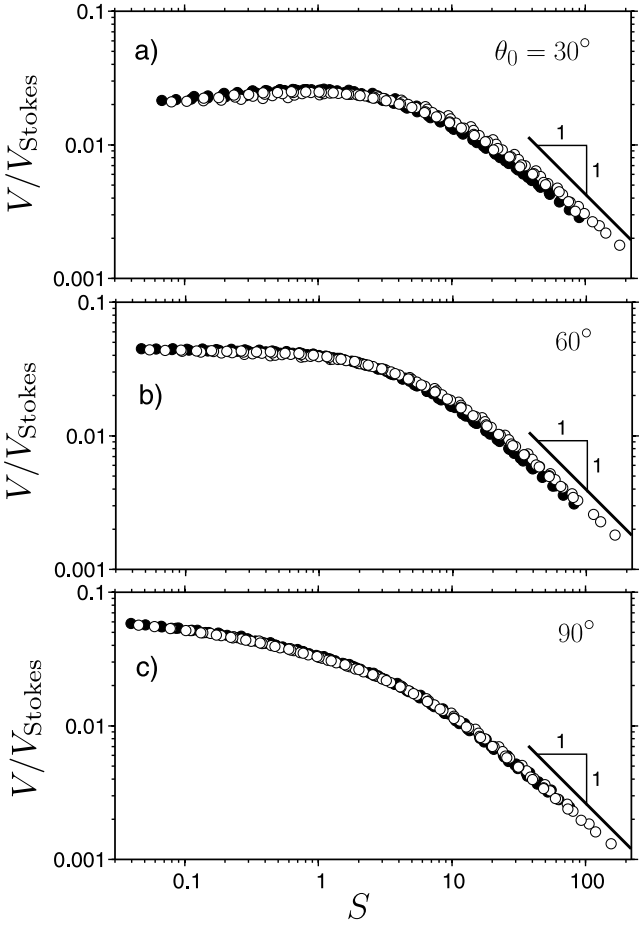

Figure 7. Dimensionless sinking speed V/V_{Stokes} of the slab as a function of the sheet stiffness S, for three different values of the dip θ_0. The geometry of the sheet is as shown in Fig. 1. A total of 588 numerical solutions with $L/h = 16$ are shown for $d/h = 0.1$ (open circles), $d/h = 0.2$ (black circles), and different values of γ and ℓ/h (see text).

Furthermore, the ratio of the internal and external viscous forces acting on the slab is

$$\frac{F_2}{F_1} \sim \gamma \left(\frac{h}{\ell_b}\right)^3 \equiv S. \tag{18}$$

The quantity S is a dimensionless measure of the 'stiffness' of a subducting sheet, and plays a fundamental role in controlling its dynamics.

The above arguments suggest that it may be revealing to plot the dimensionless sinking speed V/V_{Stokes} versus S. Fig. 7 shows such plots for a suite of 588 instantaneous BEM solutions obtained with $L/h = 16$, seven different values of ℓ/h ($4 \le \ell/h \le 10$), two values of d/h (0.1 or 0.2), fifteen different values of γ ($31.7 \le \gamma \le 10^5$), and three values of θ_0 ($30°$, $60°$ and $90°$). For each value of θ_0, all the solutions collapse onto a universal curve, independently of the particular values of ℓ/h, d/h or γ. These curves exhibit two distinct limits. For large $S \gg 1$, the slope of each curve approaches asymptotically the value -1, implying that V is controlled entirely by the viscosity η_2 of the sheet. Because the sheet's resistance to bending is the primary force resisting subduction when $S \gg 1$, I shall call this the 'flexural' limit. For $S \le 1$, by contrast, the slope of the curves in Fig. 7 is (nearly) zero, indicating that V is controlled (almost) entirely by the viscosity η_1 of the outer fluid. This 'Stokes sinking' limit corresponds to the unhindered sinking of a

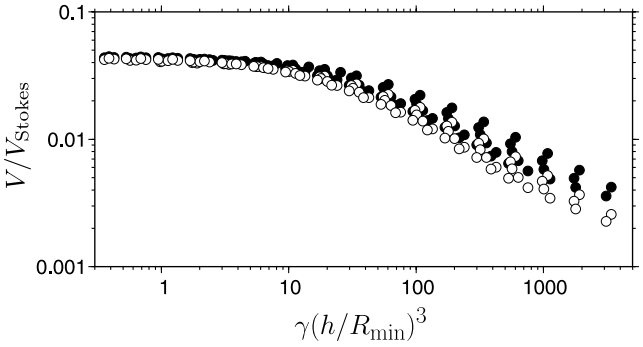

Figure 8. Same as Fig. 7b, but rescaled as a function of the modified stiffness $S^* = \gamma(h/R_{\rm min})^3$.

plate-shaped object beneath a free surface, as discussed in more detail in Appendix A.

The near-perfect collapse of the numerical data in Fig. 7 onto universal curves demonstrates that the bending length ℓ_b is the critical length scale governing the dynamics of a subducting slab. The essential point is that ℓ_b exceeds the slab length ℓ by a factor that increases with the viscosity contrast (Fig. 5) because bending stresses are significant in the region of flexural bulging seaward of the trench. For the model geometry of Fig. 1, ℓ_b depends on γ, h, ℓ, d and θ_0 in a rather complicated way that is determined in Appendix B.

The key role of the bending length ℓ_b becomes still more manifest when Fig. 7 is compared with the results of alternative rescalings. In Fig. 8, the numerical data from Fig. 7b are rescaled in terms of a modified stiffness $S^* \equiv \gamma(h/R_{\rm min})^3$ that is obtained from (18) by replacing ℓ_b by the sheet's minimum radius of curvature $R_{\rm min}$. Because the sheet's shape is described analytically by (1), $R_{\rm min} = 2\ell/3\theta_0$. When $S^* \leq 3$, all the data in Fig. 8 collapse onto the same universal curve as in Fig. 7(b), unsurprisingly because bending stresses are negligible in that limit. For $S^* \geq 10$, by contrast, the new rescaling breaks down, as indicated by the substantial scatter of the data. The length scale $R_{\rm min}$ is therefore not appropriate for characterizing the sheet's bending response. Moreover, because $R_{\rm min} \propto \ell$ when θ_0 is constant, as it is in Fig. 8, it follows that the slab length ℓ is not appropriate either.

I turn now to the scaling law that governs the plate speed U_p. The numerical solutions show that this quantity, unlike the sinking speed V, depends on the plate length L. The scaling law analogous to (13) is therefore

$$\frac{U_p}{V_{\rm Stokes}} = {\rm fct}\left(\gamma, \frac{L}{\ell}, \frac{L}{h}, \frac{d}{h}, \theta_0\right), \tag{19}$$

where the argument ℓ/h in (13) has been replaced by L/h with no loss of generality. While it is possible to determine the complete functional dependence (19), the result would be too complicated to be illuminating. Instead, consider the simpler problem of how U_p depends on γ, L/ℓ and ℓ/h with θ_0 and d/h held fixed. Fig. 9 shows $U_p/V_{\rm Stokes}$ as a function of S for $\theta_0 = 60^\circ$, $d/h = 0.2$, and various values of L/ℓ and ℓ/h. When $L/\ell = 2$ (plate length twice the slab length), the curves of $U_p/V_{\rm Stokes}$ versus S are similar in shape to those of $V/V_{\rm Stokes}$ versus S (Fig. 7). In physical terms, this means that the speed of a relatively short plate is entirely controlled by the balance of the forces F_b, F_1 and F_2 acting on the attached slab. As L/ℓ increases, however, the additional drag force exerted on the bottom of the plate by the ambient fluid becomes progressively more important relative to F_b, F_1 and F_2, so that U_p is reduced. When $L \gg \ell$, the curves of U_p versus S have strong local maxima,

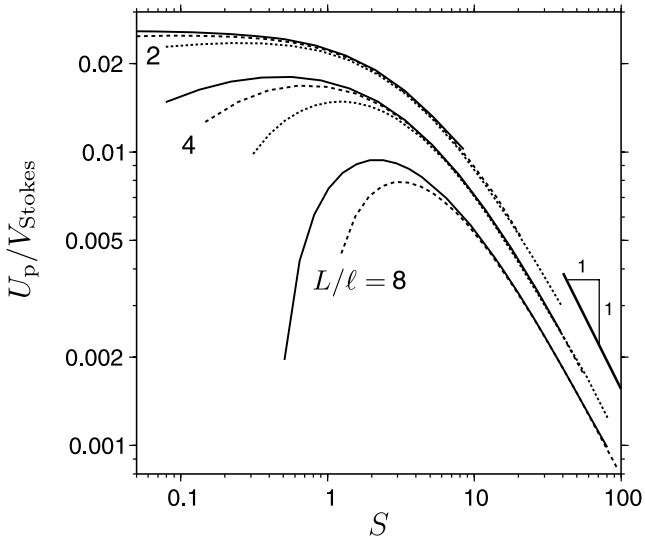

Figure 9. Dimensionless plate speed U_p as a function of S for $\theta_0 = 60^\circ$, $d_0/h = 0.2$, three values of L/ℓ (indicated) and $L/h = 32$ (solid lines), 24 (dashed lines), and 16 (dotted lines.)

implying the existence of an 'optimal' viscosity contrast $\gamma_{\rm opt}$ that gives the fastest plate speed for a given sheet geometry. For $L/\ell = 8$ and $L/h = 32$, for example, $\gamma_{\rm opt} \approx 350$.

6 MODES OF FREE SUBDUCTION

The foregoing thin-sheet analysis revealed two critical parameters that govern the dynamics of instantaneous subduction: the 'bending length' ℓ_b and the dimensionless sheet 'stiffness' S. I now show that these concepts also provide the key to understanding critical aspects of time-progressive subduction, as observed in laboratory experiments with viscous sheets sinking in a layer of fluid with a lower viscosity and a finite depth (Bellahsen *et al.* 2005; Funiciello *et al.* 2008; Schellart 2008). These experiments reveal that free subduction can occur in five different styles or 'modes' depending on the experimental parameters, as summarized in Fig. 10. The photographs in the left-hand column of Fig. 10 were taken before the sheet's leading end reached the bottom of the layer, and those in the right-hand column some time afterwards. For $\gamma \leq 100$, subduction occurs in a 'dripping' (D) mode (Fig. 10a). The slab descends nearly vertically, and its thickness varies substantially as a function of time and depth due to stretching in its upper part and shortening in its lower part. The speeds of both the plate and the trench are small in this mode. For intermediate viscosity contrasts $100 < \gamma \leq 10^4$ (approximately), three different modes are observed, depending on the plate's thickness h and width w. In the 'weak retreating' (WR) mode (Fig. 10b), the sinking slab lies down more or less flat on the bottom surface, and the trench 'retreats' to the left, that is, in the direction opposite to that of the plate motion. The 'folding retreating' (FR) mode (Fig. 10c) is similar, except that the slab folds once on the bottom of the tank before steady-state trench retreat is established. In the 'advancing' (A) mode (Fig. 10d), by contrast, the sinking slab 'bends over backwards' against the bottom of the tank, and thereafter the trench moves in the same direction as the plate. Finally, for $\gamma \gg 10^4$ subduction occurs in a 'strong retreating' (SR) mode (Fig. 10e), except if the plate is very thin, in which case the advancing mode is observed.

On the basis of his own laboratory experiments and those previously performed by others, Schellart (2008) proposed a regime

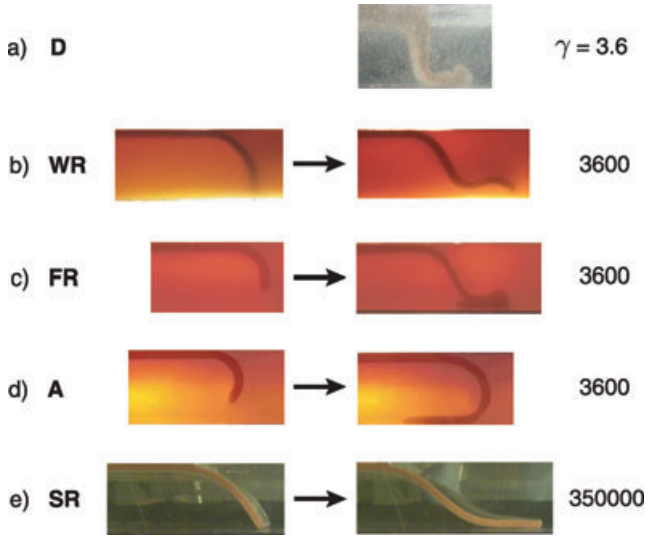

Figure 10. Modes of free subduction observed in analogue laboratory experiments. (a) 'dripping' (D) mode; (b) 'weak retreating' (WR) mode; (c) 'folding retreating' (FR) mode; (d) 'advancing' (A) mode and (e) 'strong retreating' (SR) mode. The photographs in the left-hand column were taken before the sheet's leading end reached the bottom of the experimental tank, and those in the right-hand column some time after. The viscosity contrast γ for each experiment is indicated at far right-hand side. The depths of the fluid layers are 9.4 cm for (a), 11 cm for (b)–(d) and 9.7 cm for (d). Photographs courtesy of F. Funiciello.

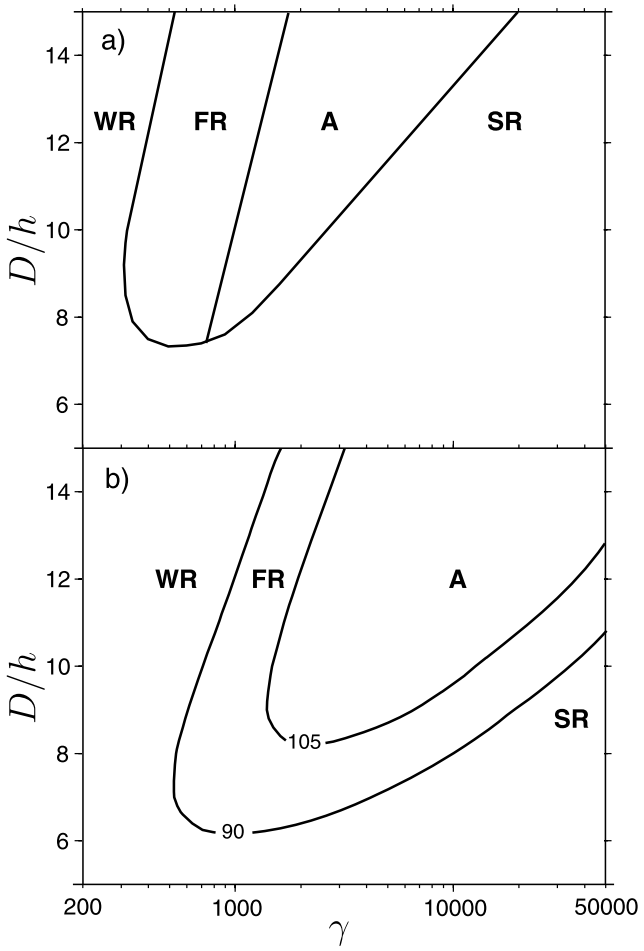

Figure 11. (a) Phase diagram showing the modes of free subduction observed in laboratory experiments as a function of the viscosity contrast γ and the ratio D/h of the layer depth to the sheet thickness (adapted from Fig. 13 of Schellart 2008). WR: weak retreating mode. FR: folding retreating mode. A: advancing mode. SR: strong retreating mode. (b) Contours of the dip θ_D (in degrees) of the tip of the slab at the time when it reaches the depth D, predicted numerically using the BEM model. The initial condition for the calculations is $\ell(0) = 0.455\ D$, $\theta_0(0) = 15^\circ$, $L/h = 16$ and $d/h = 0.2$.

diagram for the WR, FR, A and SR modes as a function of the viscosity contrast γ and the ratio D/h of the layer depth to the sheet thickness (Fig. 11a). The D mode is not included to the left-hand side of the WR field because there is a smooth transition between the two rather than a sharp boundary. The regime boundaries in Fig. 11(a) are valid for fairly narrow slabs with $w/D \approx 0.4$–2.7, and will be different for wider slabs.

Three important features of Fig. 11(a) are worth noting. First, there is no clear distinction between regimes when D/h is less than a critical value ($\approx$7.3 in Fig. 11a). Second, for a fixed value of D/h above the critical value, the modes succeed one another in an invariant order (WR, FR, A and SR) as γ increases. Third, the boundary between the WR and FR modes has a much greater slope than that between the A and SR modes.

I now show that all three of these features can be explained using the 2-D BEM model. The argument starts from the observation that there is a systematic relationship between the mode of subduction and the dip θ_D of the leading end of the slab when it first reaches the bottom of the tank. In Fig. 10, for example, the dip θ_D is less than or equal to 90° for the WR and SR modes; slightly exceeds 90° for the FR mode; and substantially exceeds 90° for the A mode. These observations suggest the working hypothesis that the mode of subduction is controlled by the dip θ_D, that is, by the amount of bending the sheet undergoes during its initial descent through the fluid layer.

To test this hypothesis quantitatively, I use the BEM model to calculate the dip θ_D as a function of γ and H/d. Fig. 11(b) shows the contours $\theta_D = 90^\circ$ and $\theta_D = 105^\circ$ of that function. Their shapes are remarkably similar to the shapes of the boundaries in the regime diagram of Fig. 11(a): each contour exists only above a minimum value of D/h, and the slope of its left-hand branch is much larger than that of its right-hand branch. The symbols WR, FR, A and SR in Fig. 11(b) indicate the subduction modes to which the different portions of the diagram correspond, assuming in accord with Fig. 10 that the WR/FR and FR/A boundaries are roughly at $\theta_D = 90^\circ$ and 105°, respectively. Fig. 11(b) thus predicts that the modes WR, FR, A and SR should be observed in that order as the viscosity contrast γ is increased for fixed D/h, in agreement with Fig. 11(a). If however D/h is less than a critical value $\approx$6.2–7.3, the dip θ_D never reaches 90°. The trench therefore retreats for any value of γ, and there is no distinction between the WR and SR modes.

If it is true that the FR mode corresponds roughly to dips $\theta_D \in [90^\circ, 105^\circ]$, then Fig. 11(b) would seem to imply that FR should be observed not only between WR and A, but also for higher values of γ between A and SR. There is no experimental evidence for this to my knowledge. The most likely reason is simply that a more viscous sheet is harder to fold than a less viscous one, which suppresses the 'second' FR mode between A and SR. However, a proper test of this hypothesis would require a more realistic 3-D model with a mantle layer of finite depth.

There are of course significant quantitative differences between Figs 11(b) and (a), the most obvious being that the contours in

Fig. 11(b) are shifted to higher values of γ relative to the regime boundaries in Fig. 11(a). The idealized 2-D character of the BEM model is only one among several reasons for this that are discussed in more detail in the Discussion below. However, the qualitative similarity between Figs 11(a) and (b) strongly supports the conclusion that the BEM model captures the essential physical mechanism responsible for mode selection in free subduction.

This conclusion is illustrated in a more visually striking way in Fig. 12, which shows the shape of the sheet as a function of γ at the time when its leading end reaches a fixed depth $D = 9.17h$ (the depth of the fluid layer in the majority of the laboratory experiments of Bellahsen *et al.* 2005). For $\gamma = 20$, subduction occurs in the dripping (D) mode (Fig. 10a). For $\gamma = 100$, $\theta_D < 90^\circ$, and so the WR mode will be observed. The dip θ_D then increases further, reaching 90° for $\gamma = 580$ and 103° for $\gamma = 1000$. Subduction should therefore occur in the FR mode in these two cases, although it should be remembered that the BEM model cannot model folding explicitly because it has no bottom boundary. For $\gamma = 5000$, θ_D significantly exceeds 90°, and so the subsequent subduction will occur in the A mode. Finally, $\theta_D \leq 90^\circ$ for $\gamma \geq 21\,400$, and so subduction will occur in the SR mode.

In closing, it is important to emphasize that both the laboratory and numerical results presented in this section are influenced by the choice of the initial condition. In the BEM calculations presented above, I chose a uniform initial condition in order to isolate the effect of the viscosity contrast γ. A more systematic study of the influence of the initial condition in the BEM models is performed in Appendix C, where it is shown that the evolution of the subducting sheet depends only on the initial bending length $\ell_b(0)$ and the initial dip $\theta_0(0)$ of the protoslab (Fig. C2.) Fig. C1 presents the same results as a function of γ, and suggests by analogy that the horizontal position of the contours in Fig. 11(b) can vary by a factor 2–3 in γ for a reasonable range of variation of the initial conditions. But the overall shapes of the contours remain unchanged, and so the numerical prediction of the mode sequence WR–FR–A–SR as a function of increasing viscosity contrast is robust.

7 GEOPHYSICAL APPLICATION

Applying the model studied here to real subduction systems requires caution for at least two reasons. First, the BEM model is a highly oversimplified representation of geophysical reality that neglects numerous potentially important factors including three-dimensionality, mantle viscosity stratification, non-linear rheology, heat transport and mineralogical phase changes. Second, several of the critical quantities predicted by the model are difficult to observe directly in real subduction zones: these include the slab sinking speed V, the bending length ℓ_b, and the sheet stiffness S.

However, the BEM does predict several other quantities that can be compared directly with observations. As a first example, consider the sheet's minimum radius of curvature $R_{\min}$. As the comparison of Figs 7 and 8 shows, $R_{\min}$ is not the fundamental lengthscale that characterizes the bending response of the sheet. Nevertheless, $R_{\min}$ is still a useful measure of the finite bending strain experienced by the sheet during subduction. Although $R_{\min}$ is a function of time in general, Fig. 6 suggests that it tends towards a roughly constant (i.e. slowly varying) value that depends on the viscosity contrast γ. To quantify this dependence, I use the BEM model to determine $R_{\min}(\gamma)$ at the time when the tip of the slab reaches a depth $D = 8.25h$ ($= 660$ km for $h = 80$ km) starting from the initial condition shown in Fig. 12(a). That initial condition was chosen to ensure that the initial value of $R_{\min}/h$ ($= 10.2$) significantly exceeds the final value for all viscosity contrasts $\gamma \in [100, 30\,000]$. Fig. 13 shows that the final value of $R_{\min}(\gamma)$ follows roughly the power law

$$R_{\min} \approx 0.50 h \gamma^{0.25}. \tag{20}$$

The scaling relation (20) can now be used in conjunction with published estimates of $R_{\min}$ to constrain the effective value of γ for subducting plates on Earth. Heuret (2005) and Wu *et al.* (2008) estimated $R_{\min}$ for 207 subduction transects, and found $R_{\min} = 100$–1300 km with a mean value 390 ± 190 km. To compare these data with the BEM model predictions, I first calculate the corresponding values of the normalized curvature radius $R_{\min}/h(\tau)$, where $h(\tau)$ and τ are the thickness and age,

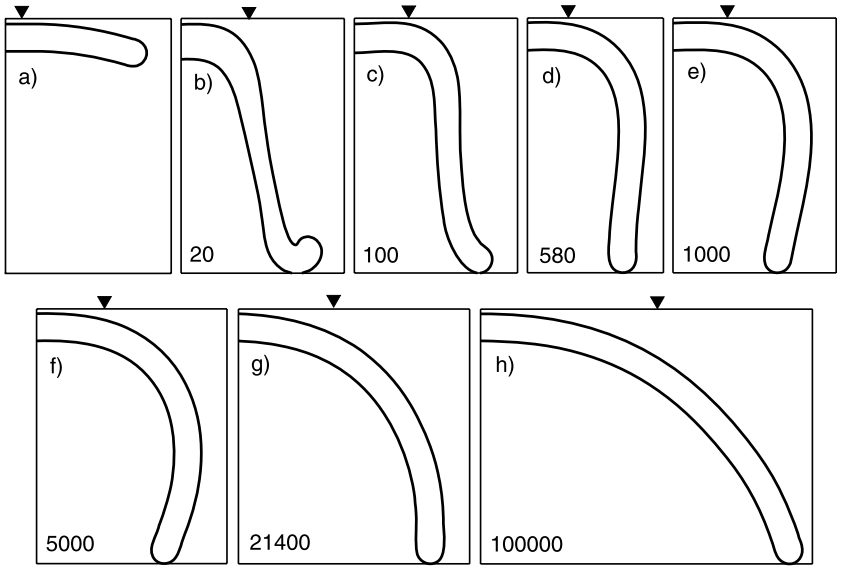

Figure 12. Shapes of subducting viscous sheets that have reached a depth $D = 9.17h$, starting from the initial conditions $L(0) = 16h$, $d/h = 0.2$, $\ell(0) = 4h$ and $\theta_0(0) = 15^\circ$ shown in panel a). The viscosity contrast γ is indicated at the lower left-hand corner of panels (b)–(h). The inverted triangles indicate the initial position of the trench.

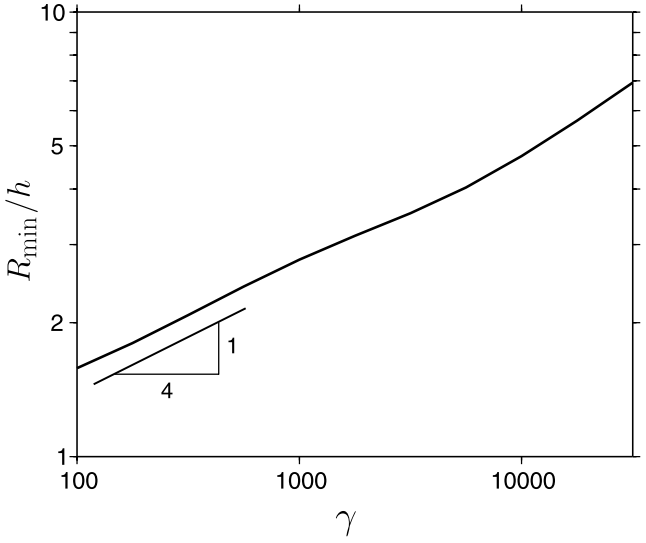

Figure 13. Minimum radius of curvature $R_{\min}$ of a subducting sheet at the time when its tip reaches a depth $D = 8.25h$, as a function of the viscosity contrast γ. The initial condition is the same as in Fig. 12(a).

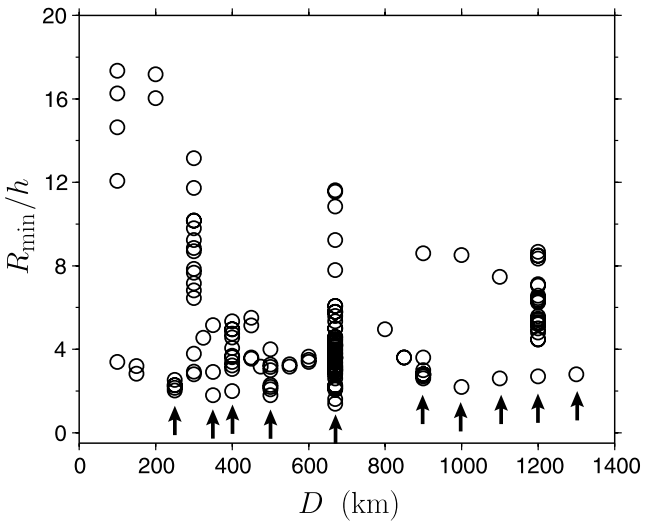

Figure 14. Normalized minimum radius of curvature $R_{\min}/h$ of subducting slabs on Earth as a function of the slab's maximum depth D (data from Wu *et al.* 2008). Arrows indicate the data points used to estimate the global minimum value of $R_{\min}/h$.

respectively, of the subducting lithosphere at the trench. I assume $h(\tau) = \min(11.2\sqrt{\tau}, 100)$ with h in km and τ in Ma, corresponding to a lithosphere that thickens conductively until it reaches its maximum thickness $h = 100$ km at $\tau = 80$ Ma. Fig. 14 shows $R_{\min}/h$ as a function of the slab's maximum depth D for all the subduction transects of Wu *et al.* (2008) for which estimates of all three parameters $R_{\min}$, τ and D are available. Despite the substantial scatter of the data, the maximum value of $R_{\min}$ at a fixed depth D clearly decreases systematically as D increases. This is consistent with the intuitive expectation, confirmed by the curves of $R_{\min}(t)$ in Fig. 6, that a slab which has been subducting longer (i.e. which has penetrated more deeply) will have a smaller $R_{\min}$, all else being equal. Furthermore, the fact that $R_{\min}$ decreases towards a γ-dependent asymptotic value at long times means that only the smallest values of $R_{\min}$ are relevant for constraining γ. A rough estimate of the 'minimum' $R_{\min}/h$ in Fig. 14, obtained by averaging the values indicated by arrows, is 2.05 ± 0.33. The scaling relation (20) then implies $\gamma \in [140, 510]$.

Another quantity predicted by the BEM model that can be compared with observations is the subduction rate $\dot{\ell}$. As an example, consider the curve $\dot{\ell}(t)$ from Fig. 3(a), which corresponds to a viscosity contrast $\gamma = 10^2$. Noting that $\ell(0) = 4h$ for that simulation and assuming $h = 100$ km, $\eta_1 = 10^{21}$ Pa s and $\Delta\rho = 65$ kg m^{-3}, one finds from (10) that $V_{\text{Stokes}} = 80$ cm yr^{-1}. The subduction rate $\dot{\ell}$ in Fig. 3(a) thus increases from $\approx$1.6 cm yr^{-1} at $t = 0$ to $\approx$7.7 cm yr^{-1} at $t = 28.5\eta_1/hg\Delta\rho$. That range of values is quite reasonable for subduction on Earth.

8 DISCUSSION

The first main result of this study is the identification of the length scale that characterizes the bending response of a subducting viscous sheet: the 'bending length' ℓ_b. In general, ℓ_b is defined as the length of the portion of the sheet's midsurface where the curling rate $\dot{K}$ (or equivalently, the bending moment) is significantly different from zero. However the precise definition of the endpoints of this portion of the midsurface is to some degree arbitrary. In this study, I defined the 'beginning' of the curling portion as the point where $\dot{K}(s) = 0$ within the region of flexural bulging (Fig. 5), but other choices (e.g. the point further seaward where $|\dot{K}|$ has a local maximum) would have served just as well. Similarly, because the slab curls significantly over its whole length in most of the cases examined here, I defined the 'end' of the curling portion as the endpoint $s = L + \ell$ of the midsurface. However, one can imagine situations in which a different definition would be necessary, for example, a slab that has penetrated so deeply that its lowermost portion hangs vertically and deforms by extension/shortening alone (Ribe 2001, Fig. 9). In this case, the curling region does not extend to the end of the slab, and a more appropriate definition of ℓ_b would be the length of the portion of the midsurface where $|\dot{K}|$ exceeds (say) 1 per cent of its maximum value.

Whatever definition of ℓ_b is used, the curling portion of the sheet will include not only the subducted slab, but also the part of the plate seaward of the trench where flexural bulging occurs. Because the lateral extent of the bulging region depends on the viscosity contrast between the sheet and its surroundings, an explicit solution of the dynamical eq. (7) is required to determine it. The implication is that ℓ_b is a property of the sheet's (instantaneous) dynamic response to loading, and cannot be determined solely from its current geometry. The bending length is therefore of a fundamentally different character from purely geometric length scales such as the slab length ℓ or the sheet's radius of curvature R.

The need for a dynamic (rather than geometric) length scale to describe the bending response of a viscous sheet is a direct consequence of the fact that viscous fluids, unlike elastic solids, have no memory. When an initially flat elastic sheet is bent, the bending moment is proportional to the local curvature K of the midsurface, and is therefore entirely determined by the sheet's current geometry. In a viscous sheet, by contrast, the bending moment is proportional to the rate of change of the curvature, which is independent of the sheet's current geometry. More generally, the viscous forces acting on a volume of fluid are not related to its shape, but rather to the rate of change of that shape. A purely geometric lengthscale is therefore not appropriate for characterizing the response of a viscous sheet to loading. This remains true even for the special case of steady-state (in the frame of the trench) subduction, a situation that arises at long times in some laboratory experiments (e.g. Bellahsen *et al.* 2005)

and numerical models (e.g. Capitanio *et al.* 2007). The normal component W of the midsurface velocity is then identically zero, and the curling rate (15) simplifies to

$$\dot{K} = U\frac{\mathrm{d}K}{\mathrm{d}s}, \tag{21}$$

that is, the advective rate of change of the curvature following the motion of a material particle along the midsurface. Even though $\mathrm{d}K/\mathrm{d}s$ is entirely determined once the sheet's geometry is known, finding the (unique) geometry that is consistent with a steady state requires solution of the dynamical equations. The function $\mathrm{d}K/\mathrm{d}s$ is thus in a very real sense 'not purely geometric'. Note further that the length scale over which $\mathrm{d}K/\mathrm{d}s$ varies along the midsurface is precisely the bending length ℓ_b. It is distinct in principle from the sheet's minimum radius of curvature $R_{\min}$, which characterizes the *amplitude* of a function (namely, $K(s)$) rather than the scale of its arcwise variation. The correct scaling relation is therefore $\mathrm{d}K/\mathrm{d}s \sim (R_{\min}\ell_b)^{-1}$, rather than (say) $\mathrm{d}K/\mathrm{d}s \sim R_{\min}^{-2}$.

The dynamic character of ℓ_b implies that it depends on the viscosity contrast γ in addition to the parameters that define the sheet's geometry. For a model with the reference geometry of Fig. 1, dimensional analysis together with the (numerically verified) result $\ell_b \neq \mathrm{fct}\,(L)$ implies

$$\frac{\ell_b}{h} = \mathrm{fct}\left(\gamma, \frac{\ell}{h}, \frac{d}{h}, \theta_0\right), \tag{22}$$

where the dependence on the four arguments is determined in Appendix B. Other models will of course predict somewhat different scaling laws for ℓ_b. However, the general definition of ℓ_b as the length of the portion of the sheet where the curling rate $\dot{K}(s)$ is significant can be applied to any model.

The second main result, which presupposes the first, is the identification of the dimensionless sheet 'stiffness' $S \equiv \gamma(h/\ell_b)^3$, the characteristic ratio of the internal and external viscous forces acting on a subducting sheet. In consequence of this definition, $S \gg 1$ means that the sheet's deformation is controlled primarily by its own viscosity ('flexural' limit), whereas $S \leq 1$ implies that the deformation is controlled by the viscosity of the surrounding fluid ('Stokes sinking' limit.) The stiffness S is defined at every instant in time. During progressive subduction, however, S tends to decrease because the slab length ℓ, and consequently also ℓ_b, is continually increasing. The role of the external fluid therefore becomes progressively more important as subduction proceeds.

The existence of distinct 'flexural' and 'Stokes sinking' limits in subduction dynamics appears at first sight to contradict the conclusion of Capitanio *et al.* (2007) that a subducting plate always sinks with the Stokes velocity. In fact, there is no inconsistency, because the sheet stiffness S is small in the numerical models of Capitanio *et al.* (2007). The focus in that study is on the special case of steady-state subduction in which the sheet bends downward at the trench, descends obliquely through the upper mantle, and then 'unbends' to become horizontal again above the 660 km discontinuity. Capitanio *et al.* (2007) provide sufficient information to estimate S for their model 'Iso23', in which an isoviscous lithosphere with viscosity contrast $\gamma = 100$ and thickness $h = 80$ km traverses the upper mantle with an average dip that depends on the density difference $\Delta\rho$. Typical values of the bending length can be estimated directly from the images of the rate of viscous dissipation within the sheet in figs 4(A) and (C) of Capitanio *et al.* (2007), and are $\ell_b \approx$ 900 km (for $\Delta\rho = 30.1$ kg m^{-3}) and $\approx$1300 km (for $\Delta\rho = 88.7$ kg m^{-3}) The corresponding stiffnesses are $S = 0.070$ and 0.023, respectively. Capitanio *et al.* (2007) also studied a stiffer isoviscous model ('Iso24') with $\gamma = 1000$, but did not present images of the dissipation rate from which ℓ_b could be estimated. However, the BEM model shows that ℓ_b is an increasing function of γ for a given sheet geometry due to the 'flexural bulging' effect, and so it is reasonable to assume that the bending lengths for model Iso24 are not smaller than those estimated for model Iso23. Because the viscosity contrast γ for model Iso24 is 10 times that for model Iso23, the definition $S = \gamma(h/\ell_b)^3$ then implies that the stiffnesses for model Iso24 are at most 10 times those estimated for model Iso23, namely, 0.70 and 0.23. These are still small values, so it is not surprising that the slabs in the models of Capitanio *et al.* (2007) sink with the Stokes velocity.

It is important at this point to understand why both the bending length and the stiffness S are independent of the sheet's buoyancy $g\Delta\rho$. Because both fluids have negligible inertia, their densities ρ_1 and ρ_2 are dynamically irrelevant except insofar as they contribute to the buoyancy term $g(\rho_2 - \rho_1) \equiv g\Delta\rho$. Moreover, because the governing equations are linear, the instantaneous velocity at any point in space is linearly proportional to $g\Delta\rho$. The parameter $g\Delta\rho$ therefore controls only the overall amplitude of the instantaneous velocity field, and has no influence whatsoever on its spatial distribution. Both ℓ_b and S must therefore be independent of $g\Delta\rho$, which can accordingly be 'scaled out' of the problem by a suitable non-dimensionalization such as (6). A further implication of this result is that the depth at which the slab's leading end achieves a given dip (e.g. 90°; Appendix C) is independent of $g\Delta\rho$, even though the time required for the slab to reach that depth scales as $(g\Delta\rho)^{-1}$.

The third main result of this study is a new hypothesis for the cause of the different modes of free subduction observed in laboratory experiments (Bellahsen *et al.* 2005; Funiciello *et al.* 2008; Schellart 2008). Photographs from those experiments suggest that the mode of steady-state subduction observed at long times might be controlled by the dip θ_D of the leading end of the slab when it reaches the bottom of the ambient fluid layer. To evaluate this hypothesis, I used the BEM model to calculate θ_D numerically as a function of the viscosity contrast γ and the ratio D/h of the layer depth to the plate thickness. The contours of the function $\theta_D(\gamma, D/h)$ strongly resemble the boundaries in the experimentally constrained regime diagram of Schellart (2008), supporting the idea that the mode of subduction is controlled by the amount of bending the slab undergoes during its initial descent through the ambient fluid layer. In particular, the BEM model explains why the modes WR–FR–A–SR always appear in that order as γ increases at a fixed value of D/h. A curious and hitherto unexplained feature of this sequence is that the trench advances (mode A) only for values of γ in an intermediate range, whereas it retreats if γ is either lower (modes WR and FR) or higher (mode SR). The physical cause of this behaviour is that θ_D can fail to reach large values $\geq$90° for two opposite reasons: either because the slab is too weak to overcome the resistance of the 'mantle wind', or because it is too strong to bend sufficiently over the depth ($= D$) available to it. Still another observation that the BEM model explains is why the A mode can be observed at very high values of γ if the plate is thin (e.g. Funiciello *et al.* 2008). This is direct consequence of the expression $S = \gamma(h/\ell_b)^3$ for the slab's stiffness, which depends much more strongly on h than on γ. As a result, the slopes of the right-hand branches of the contours in Fig. 11(b) are very small, implying that it easy to move from the SR mode to the A mode by reducing h by a fairly small factor.

Despite the striking similarity between Schellart's (2008) regime diagram (Fig. 11a) and the predictions of the BEM model (Fig. 11b),

significant quantitative differences between the two are obvious. There are several reasons for this, involving limitations of both the laboratory experiments and the BEM model. On the experimental side, the regime diagram of Fig. 11(a) is only valid for fairly narrow slabs, and no longer applies when $w > 4D$. An additional source of experimental uncertainly arises from the initial condition, which is generally difficult to control in the laboratory. The main limitation on the numerical side is the highly idealized character of the model problem, in which the sheet is strictly 2-D and the ambient fluid infinitely deep. Two-dimensionality means that the slab has no lateral edges, so that the ambient fluid displaced by its motion ('return flow') is constrained to flow around its leading edge. The viscous drag (per unit length parallel to the trench) exerted on the slab by the ambient fluid is thereby increased, with the consequence that a 2-D sheet behaves more stiffly than one with a finite width (all else being equal). The effect is further enhanced by the presence of a bottom boundary, which increases the drag even more by hindering flow around the slab's leading edge. The conjunction of these two effects is probably the main reason why the contours in Fig. 11(b) are shifted to higher values of γ relative to the regime boundaries in Fig. 11(a).

While the agreement between Figs 11(a) and (b) could certainly be improved by using a 3-D numerical model with a fluid layer of finite depth, it is more important to understand why the idealized BEM model succeeds as well as it does. First, the stiffness $S = \gamma(h/\ell_b)^3$ tends to be large in the initial stages of subduction because the bending length ℓ_b is small. Thus even if the slab has a finite width w, its initial evolution will be dominated by its internal resistance to bending, and will 'feel' neither the ambient flow nor the presence of a bottom boundary. Second, even after the slab begins to feel the ambient mantle, most of the return flow will still go around its leading edge as long as (1) the slab's length ℓ is much less than its width w and (2) its depth of penetration is much less than the layer depth. Under these conditions, the external flow will be quasi-2-D except near the slab's lateral edges. Together, these two reasons imply that the idealized 2-D BEM model describes well the slab's early evolution. That description of course breaks down progressively as the slab nears the bottom boundary, forcing a greater proportion of the return flow to go around its sides. However, the result is only a quantitative modulation of the evolutionary trajectory established in the early stages, rather than qualitatively new behaviour. It is therefore not surprising that the predictions of the idealized model (Fig. 11a) reproduce the major features of the laboratory-based regime diagram (Fig. 11b).

I noted previously that the sheet/mantle density contrast is irrelevant to the dynamics of a linear system such as the BEM model studied here. Accordingly, the foregoing discussion of regime diagrams made no reference to $\Delta\rho$. However, this appears at first sight grossly to contradict the results of laboratory experiments (Bellahsen *et al.* 2005) and 3-D numerical experiments (Stegman *et al.* 2009) in which the mode of steady-state subduction clearly depends on $\Delta\rho$. Despite appearances, there is no contradiction, because the laboratory experiments and the 3-D numerical setup, unlike the BEM model, are both non-linear systems in which the velocity $\boldsymbol{u}$ is not proportional to the driving buoyancy $g\Delta\rho$. In laboratory experiments, the non-linearity is due to the presence of surface tension; in the 3-D numerical models of Stegman *et al.* (2009), on the other hand, it arises from the use of a yield stress to get the plate to subduct. In such non-linear systems, it is impossible to non-dimensionalize the underlying governing equations in such a way as to 'scale out' the quantity $g\Delta\rho$. As a result, one or more dimensionless groups involving $g\Delta\rho$ necessarily play a role in the dynamics. For laboratory experiments, the relevant group is the (inverse) Bond number

$$Bo^{-1} = \frac{\sigma}{h^2 g \Delta\rho}, \tag{23}$$

where σ is the coefficient of surface tension. Using a value $\sigma = 78$ dyne cm^{-1} appropriate for sugar syrup (Chiu-Webster & Lister 2006, Appendix A) and all combinations of values of $\Delta\rho$ and h from table 2 of Bellahsen *et al.* (2005), one finds $Bo^{-1} \in [0.37, 2.2]$. The fact that $Bo^{-1} = O(1)$ implies that surface tension cannot be neglected, and the significant variation of Bo^{-1} among experiments explains why different modes of subduction are observed for different values of $\Delta\rho$. For the numerical setup of Stegman *et al.* (2009), the relevant dimensionless group is

$$\Pi = \frac{\tau}{hg\Delta\rho}, \tag{24}$$

where τ is the yield stress. Using all combinations of values of $\Delta\rho$ and 'h_{plate}' $(= h)$ from table 2 of Stegman *et al.* (2009) together with their value $\tau = 48$ MPa, one finds $\Pi \in [0.06, 1.85]$. Here again, the magnitude $[= O(1)]$ and range of variation of the dimensionless parameter explains why the mode of subduction is observed to depend on $\Delta\rho$. More generally, these results imply that if the system under study is non-linear, the dimensionless parameter reflecting the non-linearity (Bo^{-1}, Π, etc.) must be varied systematically in order to obtain a complete regime diagram for the subduction modes.

Two additional aspects of the model results deserve further comment. The first concerns the relationship among the several different velocities (and velocity components) that have been introduced during the course of this study: the vertical velocity of the slab tip ('sinking speed') V, the plate velocity U_p, the subduction rate $\dot{\ell}$, the horizontal component u_1^{tip} of the velocity of the slab tip, and the trench velocity $U_{\text{trench}} \equiv U_p - \dot{\ell}$. Of these, only V is independent of the plate length L; all the others depend on L to some extent. The physical reason for this is that V is controlled entirely by the local balance of forces acting on the slab (buoyancy, bending resistance and mantle traction) whereas U_p, $\dot{\ell}$, U_{trench} and u_1^{tip} are all influenced in addition by the viscous drag on the base of the plate. V is therefore independent of all the other velocities, a fact I exploited to determine the universal scaling law it obeys (Fig. 7.) By contrast, U_p, $\dot{\ell}$ and u_1^{tip} are not independent of one another, because each depends on the values of all five dimensionless parameters in the problem (γ, ℓ/h, d/h, θ_0, L/h.)

The second point that needs emphasizing concerns the role of the (arbitrary) initial conditions. In the numerical models studied here, as well as in most laboratory experiments on free subduction, the initial geometry comprises a short 'proto-slab' that can be characterized by its length $\ell(0)$ and dip $\theta_0(0)$. The BEM model shows that the sheet's subsequent evolution depends to a significant degree on these parameters (see Appendix C, especially Fig. 15). In the case of laboratory experiments, the attendant uncertainties are magnified by the difficulty of controlling the initial conditions precisely. According to F. Funiciello (personal communication, 2009), the initial dip θ_0 of the slab typically varies within the range 20–30°, and the initial depth of the slab tip within the range 2–3 cm. This variability needs to be taken into account when interpreting experimental results. More generally, the importance of the initial conditions implies that the time-invariant model parameters γ, h, D and w are not by themselves sufficient to determine the subduction mode, and consequently that no 'universal' regime diagram exists. In light of this inherent uncertainty, I have chosen here to focus on physical mechanisms and parameters (ℓ_b, S, etc.) whose relevance is independent of initial conditions.

I close by pointing out an implication of the results obtained here for subduction on Earth. In Section 7, I used Wu *et al.*'s (2008) global compilation of the minimum curvature radii of subducted slabs to estimate an effective viscosity contrast $\gamma \in [140, 510]$ for slabs in the mantle. This range of values is consistent with the nearly identical estimate $\gamma \in [150, 500]$ of Funiciello *et al.* (2008), even though the latter was based on an entirely different data set (trench/subducting plate velocity ratios.) It is also consistent with the estimate $\gamma \leq 300$ of Wu *et al.* (2008), based on yet another independent data set (observed relative plate motions.) This remarkable agreement among the results of different approaches is encouraging. Its far-reaching implication for the Earth is that γ is too low to permit the occurrence of the A (trench advancing) subduction mode, which requires $\gamma \geq 750$ (Fig. 11a.) This conclusion may seem at first sight to contradict the well-documented result that many trenches on Earth are currently advancing, regardless of the reference frame chosen (e.g. Heuret & Lallemand 2005). However, there is in fact no good reason to suppose that an advancing trench on Earth corresponds to the A mode as observed in the laboratory. On the contrary, there is a good reason to doubt it: the near-total absence of tomographic evidence for the typical 'bent over backwards' shape of a sheet undergoing A-mode subduction (Fig. 10d). This fact strongly suggests that trench advance on Earth has some other cause than a 'rollover'-type interaction of the slab with the 660-km discontinuity. One possibility is that the distribution of advancing and retreating trenches on Earth is controlled by the complex interactions among the several plates, each of which behaves differently than it would if it were alone. If this is true, then models of isolated freely subducting sheets may be of limited value in understanding the motions of Earth's surface plates.

ACKNOWLEDGMENTS

I thank T. Becker, F. Capitanio, C. Conrad, A. Davaille, E. Di Giuseppe, C. Faccenna, F. Funiciello, S. Goes, B. Kaus, J. Lister, G. Morra, W. Schellart and D. Stegman for helpful discussions. F. Funiciello generously made available numerous photographs of laboratory experiments performed at the Università Roma-Tre. A 2-D boundary-element code kindly provided by M. Manga was a helpful starting point for the code written for this study. Careful reviews by C. Conrad and F. Funiciello helped greatly to improve the manuscript. This work was supported by SEDIT (INSU) and ANR grant PTECTO.

REFERENCES

Becker, T.W., Faccenna, C., O'Connell, R.J. & Giardini, D., 1999. The development of slabs in the upper mantle: insights from numerical and laboratory experiments, *J. geophys. Res.,* **104,** 15 207–15 226.

Bellahsen, N., Faccenna, C. & Funiciello, F., 2005. Dynamics of subduction and plate motion in laboratory experiments: insights into the plate tectonics behaviour of the Earth, *J. geophys. Res.,* **110,** B01401, doi:10.1029/2004JB002999.

Billen, M. & Hirth, G., 2007. Rheologic controls on slab dynamics, *Geochem. Geophys. Geosyst.,* **8,** Q08012, doi:10.1029/2007GC001597.

Buckmaster, J.D., Nachman, A. & Ting, L., 1975. Buckling and stretching of a viscida, *J. Fluid Mech.,* **69,** 1–20.

Buffett, B.A., 2006. Plate force due to bending at subduction zones, *J. geophys. Res.,* **111,** B09405, doi:10.1029/2006JB004295.

Buffett, B.A. & Rowley, D.B., 2006a. Plate bending at subduction zones: consequences for the direction of plate motions, *Earth planet. Sci. Lett.,* **245,** 359–364.

Capitanio, F.A., Morra, G. & Goes, S., 2007. Dynamic models of downgoing plate-buoyancy driven subduction: subduction motions and energy dissipation, *Earth planet. Sci. Lett.,* **262,** 284–297.

Capitanio, F.A., Morra, G. & Goes, S., 2009. Dynamics of plate bending at the trench and slab-plate coupling, *Geochem. Geophys. Geosyst.,* **10,** Q04002, doi:10.1029/2008GC002348.

Chiu-Webster, S. & Lister, J.R., 2006. The fall of a viscous thread onto a moving surface: a 'fluid-mechanical sewing machine', *J. Fluid Mech.,* **569,** 89–111.

Christensen, U.R., 1996. The influence of trench migration on slab penetration into the lower mantle, *Earth planet. Sci. Lett.,* **140,** 27–39.

Christensen, U.R. & Yuen, D.A., 1984. The interaction of a subducting lithospheric slab with a chemical or phase boundary, *J. geophys. Res.,* **89,** 4389–4402.

Conrad, C.P. & Hager, B.H., 1999. Effects of plate bending and fault strength at subduction zones on plate dynamics, *J. geophys. Res.,* **104,** 17 551–17 571.

Conrad, C.P. & Hager, B.H., 2001. Mantle convection with strong subduction zones, *J. geophys. Int.,* **144,** 271–288.

Di Giuseppe, E., van Hunen, J., Funiciello, F., Faccenna, C. & Giardini, D., 2008. Slab stiffness control of trench motion: Insights from numerical models, *Geochem. Geophys. Geosyst.,* **9,** Q02014, doi:10.1029/2007GC001776.

Enns, E., Becker, T.W. & Schmeling, H., 2005. The dynamics of subduction and trench migration for viscosity stratification, *Geophys. J. Int.,* **160,** 761–775.

Faccenna, C., Giardini, D., Davy, P. & Argentieri, A., 1999. Initiation of subduction at Atlantictype margins: insights from laboratory experiments, *J. geophys. Res.,* **104,** 2749–2766.

Faccenna, C., Heuret, A., Funiciello, F., Lallemand, S. & Becker, T.W., 2007. Predicting trench and platemotion from the dynamics of a strong slab, *Earth planet. Sci. Lett.,* **257,** 29–36.

Funiciello, F., Morra, G., Regenauer-Lieb, K. & Giardini, D., 2003a. Dynamics of retreating slabs: 1. Insights from two- dimensional numerical experiments, *J. geophys. Res.,* **108,** B42206, doi:10.1029/2001JB000898.

Funiciello, F., Faccenna, C., Giardini, D. & Regenauer-Lieb, K., 2003b. Dynamics of retreating slabs (part 2): insights from 3D laboratory experiments, *J. geophys. Res.,* **108,** B42207, doi:10.1029/2001JB000896.

Funiciello, F., Faccenna, C. & Giardini, D., 2004. Role of lateral mantle flow in the evolution of subduction system: insights from 3-D laboratory experiments, *Geophys. J. Int.,* **157,** 1393–1406.

Funiciello, F., Moroni, M., Piromallo, C., Faccenna, C., Cenedese, A. & Bui, H.A., 2006. Mapping the flow during retreating subduction: laboratory models analyzed by Feature Tracking, *J. geophys. Res.,* **111,** B03402, doi:10.1029/2005JB003792.

Funiciello, F., Faccenna, C., Heuret, A., Lallemand, S. & Becker, T.W., 2008. *Earth planet. Sci. Lett.* **271,** 233–240.

Goes, S., Capitanio, F.A. & Morra, G., 2008. Evidence of lower-mantle slab penetration phases in plate motions, *Nature,* **451,** 981–984.

Griffiths, R.W., Hackney, R.I. & van der Hilst, R.D., 1995. A laboratory investigation of effects of trench migration on the descent of subducted slabs, *Earth planet. Sci. Lett.,* **133,** 1–17.

Guillaume, B., Martinod, J. & Espurt, N., 2009. Variations of slab dip and overriding plate tectonics during subduction: insights from analogue modelling, *Tectonophysics,* **463,** 167–174.

Guillou-Frottier, L., Buttles, J. & Olson, P., 1995. Laboratory experiments on the structure of subducted lithosphere, *Earth planet. Sci. Lett.,* **133,** 19–34.

Happel, J. & Brenner, H., 1973. *Low Reynolds Number Hydrodynamics,* Noordhoff, Leyden.

Heuret, A., 2005. Dynamique des zones de subduction: Etude statistique globale et approche analogique, *PhD thesis*, Université Montpellier II.

Heuret, A. & Lallemand, S., 2005. Plate motions, slab dynamics and back-arc deformation, *Earth planet. Sci. Lett.* **149,** 31–51.

Heuret, A., Funiciello, F., Faccenna, C. & Lallemand, S., 2007. Plate kinematics, slab shape and back-arc stress: a comparison between laboratory models and current subduction zones, *Earth planet. Sci. Lett.* **256,** 473–483.

Houseman, G.A. & Gubbins, D., 1997. Deformation of subducted oceanic lithosphere, *Geophys. J. Int.,* **131,** 535–551.
Jacoby, W.R., 1973. Model experiment of plate movements, *Nature,* **242,** 130–134.
Jacoby, W.R., 1976. Paraffin model experiment of plate tectonics, *Tectonophysics,* **35,** 103–113.
Kincaid, C. & Olson, P., 1987. An experimental study of subduction and slab migration, *J. geophys. Res.,* **92,** 13 832–13 840.
Manga, M. & Stone, H.A., 1993. Buoyancy-driven interaction between two deformable viscous drops, *J. Fluid Mech.* **256,** 647–683.
Martinod, J., Funiciello, F., Faccenna, C., Labanieh, S. & Regard, V., 2005. Dynamical effects of subducting ridges: insights from 3-D laboratory models, *Geophys. J. Int.,* **163,** 1137–1150.
McKenzie, D.P., 1969. Speculations on the consequences and causes of plate motions, *Geophys. J. R. astr. Soc.,* **18,** 1–32.
Morra, G. & Regenauer-Lieb, K., 2006. A coupled solid-fluid method for modeling subduction, *Phil. Mag.,* **86,** 3307–3323.
Morra, G., Regenauer-Lieb, K. & Giardini, D., 2006. Curvature of oceanic arcs. *Geology,* **34,** 877–880.
Morra, G., Chatelain, P., Tackley, P. & Koumoutsakos, P., 2007. Large scale three-dimensional boundary element simulation of subduction, *Int. Conf. Comp. Sci.,* Part III, LNCS 4489, 1122–1129.
Ozbench, M. *et al.*, 2008. A model comparison study of large-scale mantle-lithosphere dynamics driven by subduction, *Phys. Earth planet. Int.,* **171,** 224–234.
Piromallo, C., Becker, T.W., Funiciello, F. & Faccenna, C., 2006. Three-dimensional instantaneous mantle flow induced by subduction, *Geophys. Res. Lett.,* **33,** L08304, doi:10.1029/2005GL025390.
Pozrikidis, C., 1990. The deformation of a liquid drop moving normal to a plane wall, *J. Fluid Mech.* **215,** 331–363.
Pozrikidis, C., 1992. *Boundary Integral and Singularity Methods for Linearized Viscous Flow*. Cambridge University Press, Cambridge.
Press, W.H., Teukolsky, S.A., Vetterling, W.T. & Flannery, B.P., 1996. *Numerical Recipes in Fortran 77: The Art of Scientifc Computing,* 2nd edn, Cambridge University Press, Cambridge.
Ribe, N.M., 2001. Bending and stretching of thin viscous sheets, *J. Fluid. Mech.,* **433,** 135–160.
Ribe, N.M., 2002. A general theory for the dynamics of thin viscous sheets, *J. Fluid Mech.,* **457,** 255–283.
Ribe, N.M., 2003. Periodic folding of viscous sheets, *Phys. Rev. E,* **68,** 036305, doi:10.1103/PhysRevE.68.036305.
Royden, L.H. & Husson, L., 2006. Trench motion, slab geometry and viscous stresses in subduction systems, *Geophys. J. Int.,* **167,** 881–905.
Schellart, W.P., 2004a. Kinematics of subduction and subduction-induced flow in the upper mantle, *J. geophys. Res.,* **109,** B07401, doi:10.1029/2004JB002970.
Schellart, W.P., 2004b. Quantifying the net slab pull force as a driving mechanism for plate tectonics, *Geophys. Res. Lett.,* **31,** L07611, doi:10.1029/2004GL019528.
Schellart, W.P., 2005. Influence of the subducting plate velocity on the geometry of the slab and migration of the subduction hinge, *Earth planet. Sci. Lett.,* **231,** 197–219.
Schellart, W.P., 2008. Kinematics and flow patterns in deep mantle and upper mantle subduction models: influence of the mantle depth and slab to mantle viscosity ratio, *Geochem. Geophys. Geosyst.,* **9,** Q03014, doi:10.1029/2007GC001656.
Schellart, W.P., Freeman, J., Stegman, D.R., Moresi, L. & May, D., 2007. Evolution and diversity of subduction zones controlled by slab width, *Nature,* **446** (7133), 308–311.
Schmeling, H., Monz, R. & Rubie, D.C., 1999. The influence of olivine metastability on the dynamics of subduction, *Earth planet. Sci. Lett.,* **165,** 55–66.
Schmeling, H. *et al.*, 2008. A benchmark comparison of spontaneous subduction models—towards a free surface, *Phys. Earth. planet. Int.,* **171,** 198–223.
Shemenda, A.I., 1993. Subduction of the lithosphere and back arc dynamics; insights from physical modeling, *J. geophys. Res.,* **98,** 16 167–16 185.
Stegman, D.R., Freeman, J., Schellart, W.P., Moresi, L. & May, D., 2006. Influence of trench width on subduction hinge retreat rates in 3-D models of slab rollback, *Geochem. Geophys. Geosyst.,* **7,** Q03012, doi:10.1029/2005GC001056.
Stegman, D.R., Farrington, R., Capitanio, F.A. & Schellart, W.P., 2009. A regime diagram for subduction styles from 3-D numerical models of free subduction, *Tectonophysics,* in press, doi:10.1016/j.tecto.2009.08.041.
Turcotte, D.L., McAdoo, D.C. & Caldwell, J.G., 1978. An elastic-perfectly plastic analysis of the bending of the lithosphere at a trench, *Tectonophysics,* **47,** 193–205.
Wakiya, S., 1975. Application of bipolar coordinates to the two-dimensional creeping motion of a liquid. 2. Some problems for two circular cylinders in viscous fluid, *J. Phys. Soc. Jpn.,* **39,** 1603–1607.
Watts, A.B. & Talwani, M., 1974. Gravity anomalies seaward of deep-sea trenches and their tectonic implications, *Geophys. J. R. astr. Soc.,* **36,** 57–90.
Wu, B., Conrad, C.P., Heuret, A., Lithgow-Bertelloni, C. & Lallemand, S., 2008. Reconciling strong slab pull and weak plate bending: the plate motion constraint on the strength of mantle slabs, *Earth planet. Sci. Lett.,* **272,** 412–421.
Zhong, S. & Gurnis, M., 1996. Interaction of weak faults and non-newtonian rheology produces plate tectonics in a 3D model of mantle flow, *Nature,* **383,** 245–247.

APPENDIX A: THE STOKES SINKING LIMIT

When $S \ll 1$, the dynamics of the sheet is controlled (almost) entirely by the viscosity η_1 of the surrounding mantle. The purpose of this Appendix is to show that the limit $S \ll 1$ of Fig. 7 is consistent with unhindered Stokes sinking of a plate-shaped object beneath a free surface.

The first aspect of Fig. 7 that requires comment is the small values of $V^\star \equiv V/V_{\rm Stokes} \in [0.02, 0.06]$ when $S \ll 1$. Ideally, one would like to compare these values with an analytical solution for the sinking speed of a rigid 2-D plate with an arbitrary orientation beneath a free surface, but no such solution exists to my knowledge. A useful alternative is the analytical solution of Wakiya (1975) for the sinking speed of an infinite (2-D) circular cylinder of diameter ℓ whose centre is located a depth D below the impermeable but shear traction-free surface of a fluid half-space. The appropriate Stokes velocity scale for this case is $V_{\rm Stokes} = \ell^2 g \Delta\rho/\eta_1$. Wakiya's (1975) solution then gives $V^\star = (2\alpha - \tanh 2\alpha)/32$, where $\alpha = \cosh^{-1}(2D/\ell)$. For values of $D/\ell \in [0.75, 1.0]$ corresponding to a cylinder whose mean depth below the free surface is 0.75–1.0 times its diameter, $V^\star \in [0.030, 0.051]$. Because the mean depths of the slabs in the BEM model are also comparable to their longest lateral dimension ℓ, the above results confirm that the small values of $V^\star$ at the left-hand side of Fig. 7 are consistent with Stokes sinking that is unhindered except by the 'wall effect' of the free surface.

A second striking aspect of Fig. 7 is the systematic increase of $V^\star$ as a function of the slab dip θ_0. This reflects the fact that the terminal speed of a plate-like object falling edge-on is greater than its speed falling broadside (by exactly 50 per cent for a thin circular disk in an infinite fluid; Happel & Brenner 1973). Allowing for the fact that the slabs in the BEM model are never straight, the dips $\theta_0 = 90^\circ$ and 30° correspond roughly to 'edge-on' and 'broadside' sinking, respectively, which is consistent with the increase of $V^\star$ as a function of θ_0 in Fig. 7. However, that increase (by a factor $\approx$3) is considerably larger than the factor 1.5 one would expect for a circular disk in an infinite fluid, probably because slabs with different values of θ_0 'feel' the wall effect of the free surface differently.

A final, curious aspect of Fig. 7 is the small but non-zero slope of the curves of $V^\star$ versus S for $S \ll 1$, notable especially for

$\theta_0 = 30^\circ$ and 90°. These slopes imply that V is influenced to a small degree by the sheet viscosity η_2 even when $S \ll 1$. Moreover, the positive slope for $\theta_0 = 30^\circ$ implies the seemingly paradoxical result that V increases with increasing η_2. Although the reason for this is not clear, the effect is far too small to alter the essential result that V is dominantly controlled by the mantle viscosity η_1 when $S \ll 1$.

APPENDIX B: SCALING LAW FOR THE BENDING LENGTH

Here I determine how the bending length ℓ_b depends on the model parameters γ, h, ℓ, d and θ_0. The first task is to determine the bending length in the limit $\ell = 0$ of a perfectly flat sheet with no subducted slab. In this limit, the longitudinal velocity U of the sheet's midsurface is much smaller than the normal velocity W. Moreover, the flow in the thin layer of fluid above the sheet is described by the lubrication equation $\partial_1 p = \eta_1 \partial_{22}^2 u_1$, where p is the pressure and $\partial_i \equiv \partial/\partial x_i$. Now integrate this equation subject to $u_1(x_2 = -d) = 0$ and the free-surface condition $\partial_2 u_1(x_2 = 0) = 0$ to obtain $u_1 = \partial_1 p\ (x_2^2 - d^2)/2\eta_1$. Finally, integrate the continuity equation $\partial_2 u_2 = -\partial_1 u_1$ subject to $u_2(x_2 = 0) = 0$, evaluate the result at $x_2 = -d$, and set $u_2(x_2 = -d) = W$ to obtain

$$\frac{d^3}{3\eta_1} p'' + W = 0, \tag{B1}$$

where ∂_1 has been replaced by the arclength derivative $\mathrm{d}/\mathrm{d}s$. W in turn is governed by the equation that describes the pure bending (with negligible stretching) of a thin viscous sheet, which in the small-slope limit is (Ribe 2001)

$$\frac{\eta_2 h^3}{3} W'''' + hg\Delta\rho + p = 0. \tag{B2}$$

The three terms in (B2) represent the internal stress that resists the bending of the sheet, the sheet's integrated buoyancy, and the normal stress ($\approx -p$ in the lubrication limit) exerted on the sheet by the fluid in the lubrication layer, respectively. The normal stress exerted by the fluid beneath the sheet is small by comparison and is neglected in (B2).

Combining (B1) and (B2) into a single equation for p, we obtain

$$\frac{\gamma h^3 d^3}{9} \frac{\mathrm{d}^6 p}{\mathrm{d}s^6} - p = hg\Delta\rho. \tag{B3}$$

The appropriate boundary conditions at each end of the sheet are $W'' = W''' = 0$ (vanishing bending moment and shear stress resultant) and $p = 0$, or equivalently, $p = p'''' = p'''''' = 0$. Suppose further that the sheet is effectively of infinite length, that is, sufficiently long that the bending regions at the two ends do not influence each other. Consider for definiteness the bending region at the left-hand end $s = 0$; the solution of (B3) that satisfies the boundary conditions there and is bounded as $s \to \infty$ is

$$\frac{p}{hg\Delta\rho} = -1 + \exp(-s/\ell_0) - \frac{2}{\sqrt{3}} \exp(-s/2\ell_0) \sin\frac{\sqrt{3}s}{2\ell_0}, \tag{B4}$$

where

$$\ell_0 = \left(\frac{\gamma h^3 d^3}{9}\right)^{1/6}. \tag{B5}$$

The corresponding vertical velocity W is obtained from (B1). Its value at the end of the sheet is

$$W(s = 0) = -\frac{2d^3 hg\Delta\rho}{3\eta_1 \ell_0^2}. \tag{B6}$$

Eq. (B4) shows that ℓ_0 is the fundamental length scale that controls the buoyancy-induced bending of the sheet, which is confined to within a distance $\sim\ell_0$ of the sheet's ends. Far from the ends ($s \gg \ell_0$), $p = -hg\Delta\rho$, implying that the sheet's negative buoyancy is exactly compensated by the (upward-directed) normal stress in the lubrication layer, and that no bending occurs there. The behaviour described by (B4) and (B6) corresponds to the very slow subduction of the left ('ridge') end of the sheet in Figs 2(a)–(c).

Turning now to the more realistic case $\ell > 0$, we find from the full BEM solutions that ℓ_b varies linearly with the slab length ℓ. The general scaling law for ℓ_b must therefore have the form

$$\ell_b = A\ell_0 + B(\gamma, \theta_0, d/h)\ell, \tag{B7}$$

where A is a constant. A least-squares fit using my suite of 588 numerical solutions yields $A = 3.39 \pm 0.16$. The coefficient B varies smoothly within the range 0.58–0.82 as a function of θ_0 and d/h, but depends only weakly on γ. The figure displaying these dependences is omitted to save space, but will be provided by the author upon request.

APPENDIX C: INFLUENCE OF THE INITIAL CONDITION

To quantify how progressive subduction is influenced by its initial condition, consider the parameter D_{90}, defined as the depth (>0) of the slab's leading end at the time (t_{90}, say) when its dip first reaches 90° (Fig. 4). Unlike the sinking velocity V or the plate speed U_p, which are instantaneous quantities defined at each moment in time, D_{90} describes the result of ongoing subduction during a finite time t_{90}. The plate length $L(t)$ and the slab length $\ell(t)$ and dip $\theta_0(t)$ vary continuously during this time, but because their time evolution is entirely determined by the initial conditions only their initial values $L(0)$, $\ell(0)$ and $\theta_0(0)$ are relevant. Now D_{90} is obviously not a function of t or of $\boldsymbol{x}$, and the numerical solutions show that it is nearly independent of $L(0)$. By analogy with (9), the scaling law for D_{90} must therefore have the form

$$\frac{D_{90}}{h} = \mathrm{fct}\left[\gamma, \frac{\ell(0)}{h}, \frac{d}{h}, \theta_0(0)\right]. \tag{C1}$$

Fig. C1 shows D_{90}/h as a function of γ for a subducting sheet with $L(0)/h = 16$, $d/h = 0.2$, and three different combinations of initial values of $\ell(0)/h$ (=4 or 6) and $\theta_0(0)$ (= 15° or 30°). Three features of these curves are noteworthy. First, the significant differences among the curves indicate that D_{90} depends strongly on the initial condition. Second, $D_{90} \to \infty$ when γ is below a critical value $\gamma_c \in [430, 790]$. This is because the slab's leading end is unable to attain a dip of 90° when $\gamma < \gamma_c$ due to the opposing effect of the 'mantle wind' (see Fig. 2a for an example). Finally, each of the curves exhibits a global minimum (note that D_{90} increases downwards) at a viscosity contrast $\gamma_m \in [1150, 2100]$. The existence of such a minimum implies that a slab reaching a given fixed depth can achieve a dip of 90° or greater only if its viscosity contrast lies in an intermediate range that depends on the initial condition.

Additional insight into the influence of the initial conditions can be obtained by using thin-sheet theory to rescale the curves in Fig. C1. Note first that the relevant length scale for D_{90} is not h, but rather the initial value $\ell_b(0)$ of the time-varying bending length $\ell_b(t)$. Second, one can anticipate that the relevant dependent variable is not the viscosity contrast γ, but rather the initial value $S(0)$ of the time-varying sheet stiffness $S(t)$. Finally, because thin-sheet theory considers only quantities defined on the sheet's midsurface,

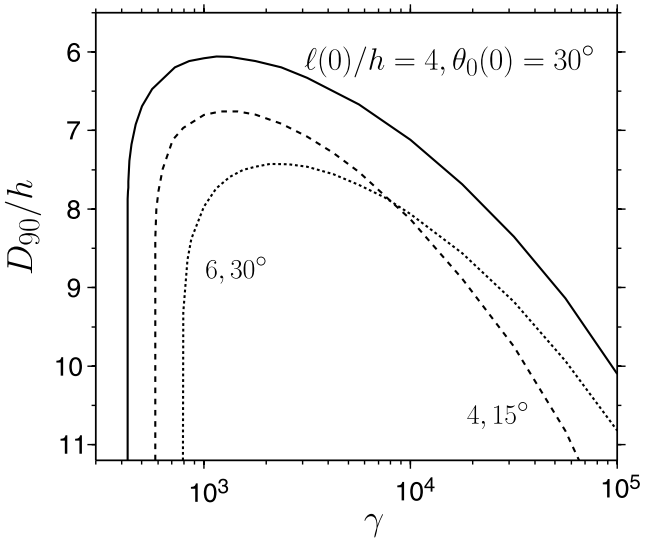

Figure C1. Depth D_{90} at which the leading end of the slab becomes vertical as a function of the viscosity contrast γ, for three combinations of initial values of $\ell(0)/h$ (= 4 or 6) and $\theta_0(0)$ (= 15° or 30°).

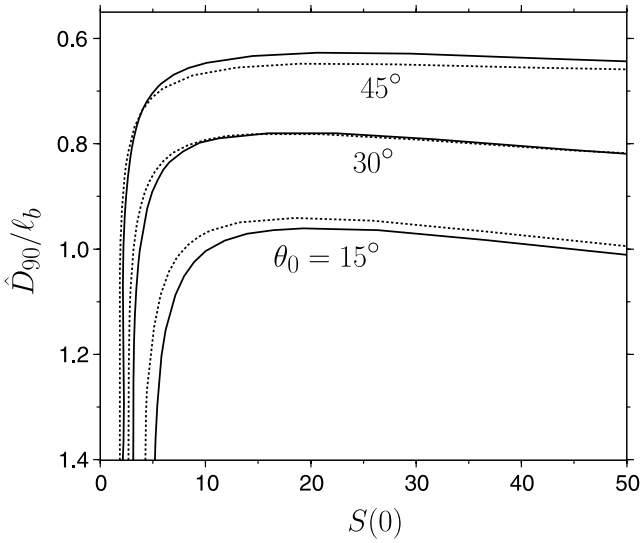

Figure C2. Midsurface deflection $\hat{D}_{90}$ (Fig. 4) at the time when the leading end of the slab first becomes vertical, as a function of the initial stiffness $S(0)$ and for three values of the initial dip $\theta_0(0)$. The solid and dotted curves are for $\ell(0)/h = 4$ and 6, respectively.

the relevant dependent variable is not the depth D_{90} of the slab's tip but rather the total downward deflection of the midsurface (Fig. 4)

$$\hat{D}_{90} = D_{90} - h/2 - 0.65h. \tag{C2}$$

Fig. C2 shows $\hat{D}_{90}/\ell_b(0)$ as a function of $S(0)$ for $\ell(0)/h = 4$ (solid lines) and 6 (dotted lines) and for three values of $\theta_0(0)$ (15°, 30°, 45°) typical of the initial dips in the laboratory experiments of Bellahsen *et al.* (2005) (F. Funiciello, personal communication, 2009). For each value of $\theta_0(0)$, the solid and dotted lines are nearly identical, indicating (nearly) complete self-similarity with respect to the initial dimensionless slab length $\ell(0)/h$. To a good approximation, therefore, the scaling law for $\hat{D}_{90}$ has the form

$$\hat{D}_{90} = \ell_b(0) G[S(0), \theta_0(0)], \tag{C3}$$

where G denotes the functional dependence shown in Fig. C2. Because $S(0)$ depends only on $\ell_b(0)$ and the (known) values of h and γ, (C3) implies that the depth D_{90} at which the slab tip becomes vertical can be predicted entirely from the initial values of the bending length $\ell_b(0)$ and the dip $\theta_0(0)$. The rescaling also clarifies the role of the initial dip by revealing that $\hat{D}_{90}$ decreases monotonically as a function of $\theta_0(0)$ (Fig. C2). This is simply because slabs with higher initial dips $\theta_0(0)$ have less rotation to accomplish before reaching the dip $\theta_0(t_{90}) = 90^\circ$.